MNRAS 000, 1–16 (2020) Preprint 5 October 2021 Compiled using MNRAS LATEX style file v3.0

On the "Lensing is Low" of BOSS Galaxies

Ying Zu[1]★
[1]Department of Astronomy, School of Physics and Astronomy, Shanghai Jiao Tong University, Shanghai 200240, China
[2]Shanghai Key Laboratory for Particle Physics and Cosmology, Shanghai Jiao Tong University, Shanghai 200240, China

Accepted XXX. Received YYY; in original form ZZZ

ABSTRACT

Recently, Leauthaud et al discovered that the small-scale lensing signal of Baryon Oscillation Spectroscopic Survey (BOSS) galaxies is up to 40% lower than predicted by the standard models of the galaxy-halo connections that reproduced the observed galaxy stellar mass function (SMF) and clustering. We revisit such "lensing is low" discrepancy by performing a comprehensive Halo Occupation Distribution (HOD) modelling of the SMF, clustering, and lensing of BOSS LOWZ and CMASS samples at Planck cosmology. We allow the selection function of satellite galaxies to vary as a function of stellar mass as well as halo mass. For centrals we assume their selection to depend only on stellar mass, as informed by the directly measured detection fraction of the redMaPPer central galaxies. The best-fitting HOD successfully describes all three observables without over-predicting the small-scale lensing signal. This indicates that the model places BOSS galaxies into dark matter halos of the correct halo masses, thereby eliminating the discrepancy in the one-halo regime where the signal-to-noise of lensing is the highest. Despite the large uncertainties, the observed lensing amplitude above 1 h^{-1}Mpc remains inconsistent with the prediction, which is however firmly anchored by the large-scale galaxy bias measured by clustering at Planck cosmology. Therefore, we demonstrate that the "lensing is low" discrepancy on scales below 1 h^{-1}Mpc can be fully resolved by accounting for the halo mass dependence of the selection function. Lensing measurements with improved accuracy is required on large scales to distinguish between deviations from Planck and non-linear effects from galaxy-halo connections.

Key words: gravitational lensing: weak — galaxies: evolution — galaxies: luminosity function, mass function — methods: statistical — cosmology: observations — large-scale structure of Universe

1 INTRODUCTION

The large-scale clustering of BOSS CMASS and LOWZ galaxies are the state-of-the-art data sets (Alam et al. 2017) that allow accurate measurements of the expansion history of the accelerating Universe and the cosmic growth of large-scale structures (Weinberg et al. 2013). Such cosmological analysis with BOSS galaxy samples relies on the accurate modelling of the galaxy-halo connection in the Universe (Wechsler & Tinker 2018). However, Leauthaud et al. (2017) recently discovered that the galaxy-galaxy lensing (hereafter g-g lensing) signal of the BOSS CMASS galaxies is significantly lower than predicted by their best-fitting model that reproduced the stellar mass function (SMF) and clustering of those galaxies. Subsequently, Lange et al. (2019) showed that a similar discrepancy between clustering and g-g lensing also exists in the BOSS LOWZ galaxy sample. Leauthaud et al. (2017) explored the impact of baryonic physics, massive neutrinos, and modifications to General Relativity (GR), but none of these effects can resolve this so-called "lensing is low" discrepancy. Therefore, "lensing is low' signals an alarming gap between the observed galaxies and the dark matter haloes evolved under GR in the Λ-dominated cold dark matter (ΛCDM) Universe described by Planck Collaboration et al. (2020).

Beyond Planck, Leauthaud et al. (2017) and Lange et al. (2019) both found that lowering the cosmological parameter $S_8 \equiv \sigma_8 \sqrt{\Omega_m/0.3}$ by $2-3\sigma$ from the Planck value can somewhat reconcile the discrepancy. However, as pointed out in Leauthaud et al. (2017), the g-g lensing measurements are dominated by non-linear scales where details of galaxy-halo connection matter the most, a significantly lower value of S_8 is therefore unlikely the favored solution unless we have thoroughly understood the systematic uncertainties in the galaxy-halo connection at the Planck cosmology. In this paper, we perform a comprehensive HOD modelling of the BOSS galaxies and carefully account for the halo mass-dependence of the BOSS target selection due to the complex colour cuts, in hopes of identifying the missing link *within* the Planck ΛCDM paradigm before exploring any new physics.

Galaxy assembly bias has been regarded as one of possible solutions. In particular, at fixed cosmology the projected clustering tightly constrains the large-scale galaxy bias, but on small scales is

★ E-mail: yingzu@sjtu.edu.cn

severely limited by the fact that no two fibres can be placed closer than $62''$ on a given plate (a.k.a., fibre collision). Meanwhile, the g-g lensing signal is limited to scales below $10\,h^{-1}$Mpc and primarily measures the one-halo term, which depends on the mean halo mass of the sample and the fraction of satellite galaxies. Therefore, the low amplitude of g-g lensing could be caused by a preference of the BOSS galaxies to reside in halos with, e.g, lower concentration, hence the higher large-scale bias (i.e., "halo assembly bias"; Sheth & Tormen 2004; Gao et al. 2005; Gao & White 2007; Jing et al. 2007). However, applying two extended HOD models that include such galaxy assembly bias effect to the CMASS sample, Yuan et al. (2020) found that their fit still strongly suggests a ∼34 per cent discrepancy between the projected clustering and g-g lensing signals. This finding is consistent with the recent work of Salcedo et al. (2020), who found no evidence for a strong galaxy assembly bias after a thorough investigation of the one and two-point galaxy statistics in SDSS.

Another possibility is the lack of proper modelling of the spectroscopic selection function of BOSS galaxies. Optimized for the Baryon Acoustic Oscillation (BAO) analysis, the BOSS target selection relies on complex sets of colour and magnitude cuts over SDSS *ugriz* photometry to efficiently select the most massive and passive galaxies, at z<0.43 for LOWZ and between z∼0.43 and 0.7 for CMASS, respectively (Reid et al. 2016). To construct a roughly "constant mass" (hence the name CMASS) sample, the selection criteria are theoretically motivated by the Maraston et al. (2009) Luminous Red Galaxy (LRG) template that describes the passive evolution of a predominantly metal-rich population (with 3 per cent of the stellar mass in old metal-poor stars). This template provides a good overall fit to the colours of massive LRGs that generally show no evidence of additional evolution beyond passive (Wake et al. 2006).

If the BOSS colour and magnitude cuts closely follow the tracks of *all* massive galaxies on the colour-magnitude diagram, one can then safely assume that the detection fraction of galaxies in BOSS depends only on their stellar mass. For instance, the best-fitting model of galaxy-halo connection adopted by Leauthaud et al. (2017) was originally derived in Saito et al. (2016), who performed a joint analysis of the projected correlation function and the galaxy SMF using subhalo abundance matching (SHAM; Conroy et al. 2006; Vale & Ostriker 2006; Shankar et al. 2006; Guo et al. 2016). They account for the stellar mass incompleteness of CMASS by down-sampling mock galaxies to match the redshift-dependent CMASS SMFs(see also Rodríguez-Torres et al. 2016). Alternatively, Guo et al. (2018) modelled the central and satellite galaxy completeness separately as two functions of stellar mass, each with a three-parameter functional form proposed in Leauthaud et al. (2016). Adopting the incompleteness conditional stellar mass function of Guo et al. (2018), Lange et al. (2019) analysed the LOWZ sample using an analytic HOD framework, and confirmed that the LOWZ galaxies also exhibit a discrepancy very similar to that in CMASS.

However, a simple passive evolution model is insufficient for describing at least some of the observed massive galaxies, depending on their star formation rates (SFRs) (Eisenhardt & Lebofsky 1987; Runge & Yan 2018; Cerulo et al. 2019). Using the Stripe 82-Massive Galaxy Catalog (S82-MGC; Bundy et al. 2015), Bundy et al. (2017) discovered that at the most massive end the SMF was dominated by galaxies with some residual star formation ($-2.7<\lg\mathrm{SFR}<-0.5$) at z∼0.6, which then became completely quiescent at lower redshifts. More interestingly, there exists a sub-population of massive galaxies with ongoing star formation($\lg\mathrm{SFR}>-0.5$) whose number density stays roughly constant with redshift. Matching the BOSS catalogue to S82-MGC, Leauthaud et al. (2016) found that many galaxies with signs of recent star formation are excluded from the CMASS sample at redshifts between 0.4 and 0.6 by the colour cuts. At z<0.4, a sliding colour cut preferentially removed some of the relatively low-mass galaxies with bluer colours from the LOWZ sample.

Therefore, the detection fraction of BOSS galaxies at fixed stellar mass should also depend on halo properties that are strongly tied to galaxy colours. In essence, this dependence is fundamentally linked to the astrophysics that governs galaxy quenching, i.e., the rapid cessation of star formation (Naab & Ostriker 2017) that leads to the blue-to-red colour transformation of galaxies. Using the colour dependence of the projected clustering and g-g lensing of SDSS galaxies as constraint, Zu & Mandelbaum (2016) explored three different phenomenological models for galaxy quenching, which tie galaxy colours to halo mass, stellar mass, and halo formation time, respectively. They found that the halo mass quenching model provides an excellent fit to the SDSS measurements, while the other two exhibit strong discrepancy between the g-g lensing and clustering of SDSS galaxies at the high-mass end (see also Mandelbaum et al. 2016; Zu & Mandelbaum 2016), in a very similar fashion to the current tension found within BOSS (see their figure 10). In this paper, we build on the `iHOD` halo quenching framework of Zu & Mandelbaum (2015, 2016, 2018) and incorporate the stellar as well as halo mass dependence of galaxy selection functions into our analytic HOD framework, in hopes of reproducing the observed low small-scale g-g lensing signal at fixed large-scale galaxy bias.

This paper is organized as follows. We briefly describe the BOSS LOWZ and CMASS data and the overlapping cluster sample in § 2, and introduce our extended HOD model in § 3. We present our main findings on the lensing-clustering discrepancy in LOWZ in § 4 and in CMASS in § 5. We conclude by summarizing our results and looking to the future in § 6. Throughout this paper, we assume the Planck 2020 cosmology Planck Collaboration et al. (2020) with Ω_m=0.315, σ_8=0.811, and h=0.6736. All the length and mass units in this paper are scaled as if the Hubble constant were $100\,\mathrm{km\,s^{-1}Mpc^{-1}}$. In particular, all the separations are co-moving distances in units of h^{-1}Mpc, and the stellar and halo mass are in units of $h^{-2}M_\odot$ and $h^{-1}M_\odot$, respectively. We use $\lg x=\log_{10}x$ for the base-10 logarithm and $\ln x=\log_e x$ for the natural logarithm.

2 DATA

2.1 BOSS LOWZ and CMASS Samples

As part of the SDSS-III programme (Eisenstein et al. 2011), BOSS (Dawson et al. 2013) measured the spectra of 1.5 million galaxies over a sky area of ∼10,000 deg^2 using the BOSS spectrographs (Smee et al. 2013; Bolton et al. 2012) onboard the 2.5-m Sloan Foundation Telescope at the Apache Point Observatory (Gunn et al. 1998, 2006). BOSS galaxies were selected from the Data Release 8 (DR8; Aihara et al. 2011) of SDSS five-band imaging (Fukugita et al. 1996) using two separate sets of colour and magnitude cuts for the LOWZ (0.15<z<0.43) and CMASS (0.43<z<0.7) samples, respectively (Reid et al. 2016). We use the Data Release 12 of the BOSS galaxy sample, which is also the final data release that includes the complete dataset of the BOSS survey (Alam et al. 2015).

Conceptually, the main difference between the LOWZ and CMASS cuts is the extension of the CMASS selection towards

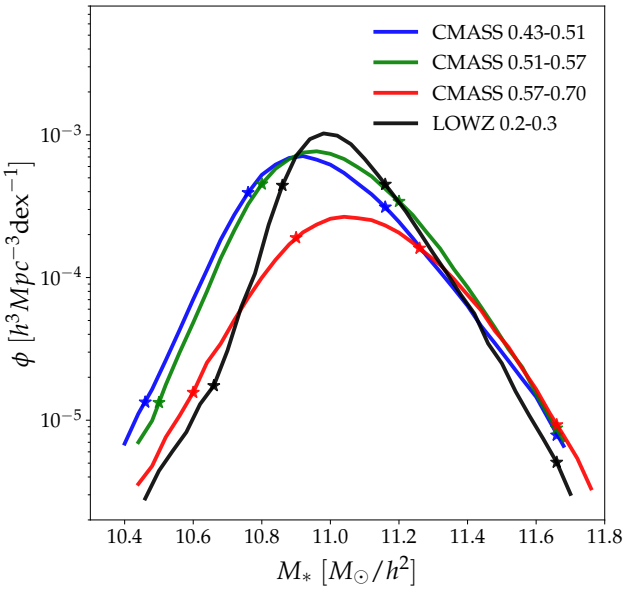

Figure 1. The stellar mass functions of the four redshift samples in our analysis, labelled by the legend in the top right corner. The four stars on each curve indicate the bin edges of the three stellar mass subsamples for which we measure the projected correlation functions. We carefully pick the stellar mass bins so that the peak of each SMF is well-contained by the intermediate mass bin.

the blue. Using high-resolution *HST* imaging, Masters et al. (2011) showed that ∼26 per cent of the CMASS galaxies in the COSMOS sample have late-type morphologies. Using an unbinned maximum likelihood approach, Montero-Dorta et al. (2016) estimated that the fraction of intrinsically blue galaxies in CMASS increases considerably as a function of redshift, from ∼36 per cent at z=0.5 to ∼46 per cent at z=0.7. Therefore, we anticipate a different halo mass dependence of LOWZ and CMASS selection functions, as well as a redshift-dependence of the parameters that describe CMASS selection.

We employ the stellar mass measurements from Chen et al. (2012), who fit the galaxy spectra over the rest-frame wavelength range of 3700−5500 Å using a principal component analysis method. In particular, we adopt the stellar mass estimates obtained by applying the Stellar Population Synthesis (SPS) model of Maraston & Strömbäck (2011) with the Kroupa (2001) Initial Mass Function (IMF) and the dust attenuation model of Charlot & Fall (2000). All the masses are aperture-corrected by applying the mass-to-light ratio within the fibre to the whole galaxy. To facilitate our comparison with the results from previous studies (e.g., Lange et al. 2019), we follow Guo et al. (2018) by reducing the Chen et al. stellar masses by 0.155 dex.

For the LOWZ galaxies, we will focus on the redshift range of z=[0.2, 0.3], for which we have a well-defined cluster catalogue from redMaPPer (Rykoff et al. 2014). As will be further discussed in § 2.2, we rely on the volume-limited sample of brightest central galaxies (BCGs) defined by redMaPPer to inform us the detection fraction of central galaxies. For the CMASS galaxies, following Leauthaud et al. (2017) we divide them into three redshift bins, z=[0.43, 0.51], z=[0.51, 0.57], and z=[0.57, 0.70], respectively. In total, we will analyse four redshift bins of BOSS galaxies that we will refer to as LOWZ 0.2−0.3, CMASS 0.43−0.51, CMASS 0.51−0.57, CMASS 0.57−0.70, respectively.

Figure 1 shows the observed SMFs of the four redshift bins, marked by the legend on the top right. The three CMASS samples all have bell-shaped SMFs, with CMASS 0.43−0.51and CMASS 0.51−0.57having higher peak amplitudes than CMASS 0.57−0.70. The bell shape is caused by the fact that the low mass portion of the SMFs suffers strong incompleteness, while the high mass portion enjoys relatively high completeness. Therefore, if the selection function is additionally modulated by halo mass, we would expect that the low stellar mass galaxies exhibit deviations from the naive prediction assuming they are randomly selected from the parent sample at fixed stellar mass. To capture such potential deviations in the clustering measurements, for each redshift bin we further divide the galaxies into three bins of stellar mass, with two bins representing the low and high mass portions of the SMF, and the intermediate stellar mass bin anchoring the peak of the SMF, respectively. We will refer to them simply as Low−M_*, High−M_*, and Mid−M_*, respectively. The bin edges we adopt are illustrated by the star symbols on each SMF curve in Figure 1 and listed below

- LOWZ 0.2−0.3: lg M_*=[10.66, 10.86, 11.16, 11.66] ,
- CMASS 0.43−0.51: lg M_*=[10.46, 10.76, 11.16, 11.66] ,
- CMASS 0.51−0.57: lg M_*=[10.50, 10.80, 11.20, 11.66],
- CMASS 0.57−0.70: lg M_*=[10.60, 10.90, 11.26, 11.66].

Intriguingly, the LOWZ 0.2−0.3 SMF shows an additional feature compared to the CMASS ones — a change of slope at lg M_*∼10.7 towards the low mass tail. This slope change suggests that the LOWZ SMF may consist of two distinctive components at the low vs. high stellar mass ends, e.g., due to different selection functions for the central and satellite galaxies. Therefore, any successful model should explain this feature in the LOWZ SMF in addition to the overall amplitude of the SMF.

We emphasize that the deliberate binning of stellar mass is crucial to our HOD analysis. In particular, the large-scale clustering of galaxies measures the weighted average of the central and satellite galaxy biases. By dividing the galaxies into stellar mass bins with drastically different levels of completeness, the large-scale clustering thus provides key information on the satellite fraction as a function of both stellar mass and completeness, helping disentangle the small-scale g-g lensing signal into central vs. satellite contributions. In comparison, Leauthaud et al. (2017) used the projected clustering of a single bin of all CMASS galaxies, while Lange et al. (2019) adopted two somewhat arbitrary stellar mass bins regardless of where the observed SMF peaks.

2.2 Brightest Central Galaxy Sample from redMaPPer Cluster Catalogue

To investigate the BOSS detection fraction of the central galaxies, we employ an SDSS cluster catalogue derived from SDSS DR8 imaging using the red-sequence-based matched-filter photometric cluster finding algorithm redMaPPer (Rykoff et al. 2014). The redMaPPer cluster catalogue measures the richness λ of satellite galaxies brighter than 0.2 L_* within an aperture ∼1 h^{-1}Mpc (with a weak dependence on λ) as its proxy for halo mass. Rykoff et al. (2014) demonstrated that the cluster catalogue is approximately volume-complete above λ=20 to z≃0.33 with excellent photometric redshift estimates ($\delta(z) = 0.006/(1+z)$). Therefore, the redMaPPer BCG sample serve as an ideal data set that allows us to *directly* mea-

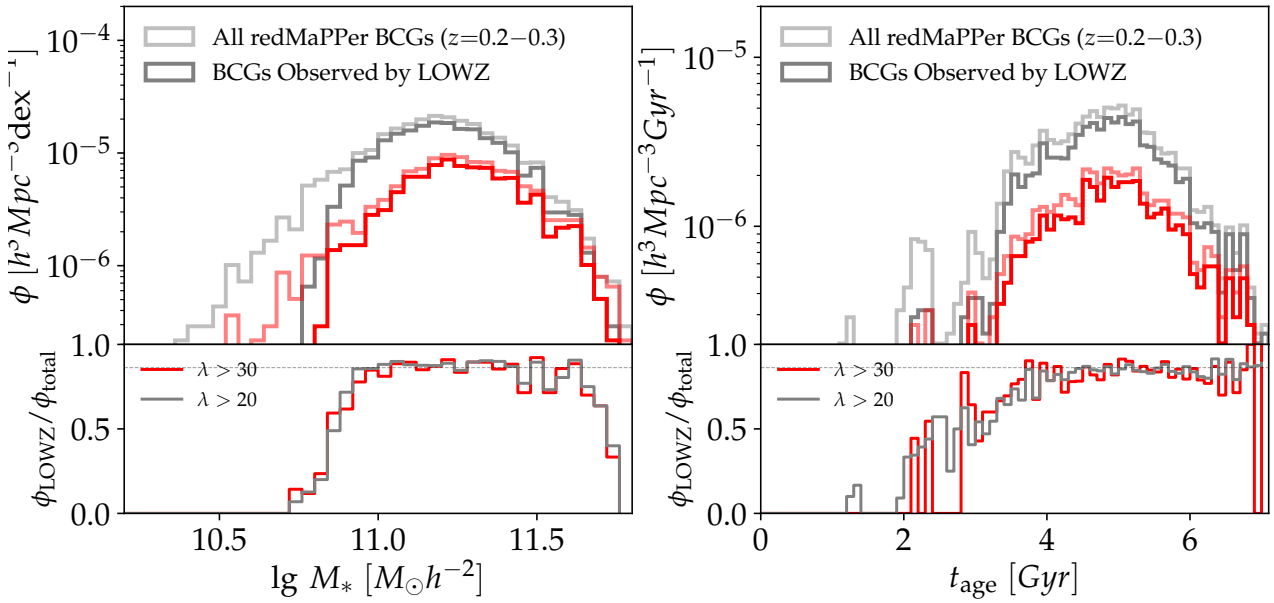

Figure 2. *Top*: Comparison between the number density distribution of BCGs of all the redMaPPer clusters (light gray and red) and those spectroscopically observed by LOWZ (dark gray and red), as functions of BCG stellar mass (left) and BCG stellar age (right), respectively. *Bottom*: The detection fraction of redMaPPer BCGs by the LOWZ spectroscopic observation, with the horizontal dotted line indicating the maximum LOWZ detection fraction of the BCGs. In each panel, gray and red histograms indicate the measurements from λ>20 and λ>30 clusters, respectively. The selection functions of BCGs show little dependence on cluster richness.

sure the BOSS detection fraction of the central galaxies of massive haloes as a function of both stellar mass and cluster richness.

We employ 3822 BCGs of the redMaPPer λ>20 clusters between z=0.2−0.3 and within the same sky area covered by the LOWZ 0.2−0.3 sample. The average halo mass of those clusters is accurately measured from weak lensing ($\simeq 1.86\times10^{14}h^{-1}M_{\odot}$; Miyatake et al. 2016; Simet et al. 2017), and their large-scale halo bias is consistent with the lensing mass. When divided by galaxy concentration, the halo assembly bias exhibited by those clusters is also in perfect agreement with that predicted by the ΛCDM at Planck cosmology (Zu et al. 2017). Therefore, at the high stellar mass end, there is no evidence an analogous "lensing is low" discrepancy (i.e., halo mass-bias discrepancy) within the volume-limited sample of redMaPPer BCGs.

However, due to the lack of spectra for the BCGs that were not observed by BOSS (788; 21% of the total sample), we do not have Chen et al. (2012) stellar mass estimates available for these objects. Thanks to the excellent photometric redshift estimates by the redMaPPer algorithm, we can derive reasonably accurate stellar masses for all the BCGs by fitting a two-component Simple Stellar Population (SSP) template to their SDSS *ugriz* photometry. Following Maraston et al. (2009), we include a dominant component (97 per cent) of a solar metallicity population, with 3 per cent of a metal-poor (Z=0.008) population of the same age. We utilized the `EzGal` software (Mancone & Gonzalez 2012) and adopt the Bruzual & Charlot (2003) SSP model and a Chabrier (2003) IMF for the fits. For the aperture correction, we carry out the fit on extinction-corrected model magnitudes that are scaled to the i-band c-model magnitudes.

The SSP and IMF assumptions are different from the Chen et al. (2012) fits, so the BCG stellar masses inferred from `EzGal` are systematically lower than the original Chen et al. (2012) values by ~0.2 dex, hence ~0.045 dex lower than the values adopted in our analysis (with the 0.155-dex offset). There is also a scatter of ~0.1 dex between the `EzGal` and Chen et al. (2012) masses, mainly due to the difference in star formation histories. The difference between the two stellar mass estimates are not important because our goal in this Section is to investigate the functional forms of the BOSS selection function and its dependence on the host halo mass proxy λ, which should be independent on the exact values of the stellar mass estimates.

The top panels of Figure 2 show the cluster number density distributions as functions of stellar mass (left) and stellar age (right) of the BCGs. In each panel, the gray histograms show the results for all the clusters with λ above 20, while the red histograms with λ above 30. Within each colour, the light and dark-colour histograms indicate the distributions of all BCGs and those spectroscopically observed by LOWZ, respectively. The bottom panels show the LOWZ detection fraction of all the BCGs as the ratios of the dark over light-colour histograms.

For the detection fraction as a function of stellar mass on the bottom left panel of Figure 2, there is a plateau of maximum detection efficiency of ~86% at 11< lg M_*<11.4 (`EzGal` mass estimates), which declines towards zero at both ends of the stellar mass distribution. The plateau is probably due to some photometric effects like the masking that reduces the effective area of the LOWZ target selection. The cut-offs can be both described by the functional forms introduced by Leauthaud et al. (2016), as shown by the gray dashed curve in the bottom panel of Figure 3, with some slight shift due to the difference between the Chen et al. (2012) and `EzGal` stellar mass estimates. The low-mass cut-off is relatively sharp, indicating that the LOWZ target selection does a great job selecting a stellar mass-thresholded sample of central galaxies. More important, the cut-off is roughly independent of λ (compare red to gray), indicating that the selection is insensitive to halo mass, at least in the cluster mass regime. Meanwhile, it is unclear what caused the cut-off at

the high-mass end, probably due to some rejuvenated star formation in the most massive systems (Runge & Yan 2018). The impact on our analysis is however negligible because the number of galaxies affected by this high-mass cut-off is very low.

The bottom right panel of Figure 2 shows the two detection fractions as functions of stellar age for the λ>20 (gray) and λ>30 (red) samples. The stellar age of each BCG is derived during the `EzGal` fitting to broad-band colours assuming an SSP at some birth redshift, and is therefore more meaningful when used as a measure of the relative age among the stellar population than absolute. Similar to the stellar mass dependence, the stellar age dependence also reaches a maximum detection efficiency of ∼86% at $t_{\rm age}$>5 Gyrs, and slowly declines into zero across of spread of $\Delta\, t_{\rm age}$∼4 Gyrs. This confirms our expectation from § 1 that the incompleteness is primarily due to the blueward deviation from the colour of a passively evolving galaxy due to star formation. Such deviation is also insensitive to halo mass, as the rich clusters exhibit similar stellar-age selection effects than the poor ones (compare red to gray).

To summarize, the selection function of central galaxies of massive clusters reaches a maximum of ∼86% for the high-stellar mass, old-age population, with a sharp cut-off at lg M_*∼10.9 that unfolds into a slow decline across a span in stellar age of 4 Gyrs. More important, such behavior is relatively insensitive to cluster richness, hence unlikely a strong function of halo mass. Therefore, in our analysis with both the LOWZ and CMASS samples, we will extrapolate our findings among the redMaPPer clusters into the low mass regime and assume that the detection fraction of central galaxies is a function of only stellar mass.

2.3 Large-scale Structure Measurements

For each of the redshift bins, we jointly analyse the observed SMF (Figure 1), the g-g lensing of the total galaxy sample, and the projected correlation functions of the three stellar mass subsamples defined in § 2.1 (also see the stars in Figure 1). We employ the g-g lensing signal of the LOWZ 0.2−0.3 sample measured by Lange et al. (2019), and that of the CMASS 0.43−0.51, CMASS 0.51−0.57, and CMASS 0.57−0.70 samples measured by Leauthaud et al. (2017), respectively. Below we briefly describe the measurements of the projected auto-correlation functions for the stellar mass subsamples, and refer readers to Leauthaud et al. (2017) and Lange et al. (2019) for the technical details of the g-g lensing measurements.

We measure the projected auto-correlation function w_p as the integration of the redshift-space correlation function $\xi^{rs}(r_p, r_\pi)$ as follows

$$w_p = \int_{-r_\pi^{\rm max}}^{+r_\pi^{\rm max}} \xi^{rs}(r_p, r_\pi)\, {\rm d}r_\pi, \tag{1}$$

where r_p and r_π are the projected and line-of-sight separation of galaxy pairs, respectively, and $r_\pi^{\rm max}$ is the integration limit along the line of sight, which we set to be 100 h^{-1}Mpc to minimize the redshift space distortion effects. To make sure that the spatial correlation signal is from a contiguous region on the sky, we only use the BOSS observations of the North Galactic Cap. We adopt the Davis-Peebles estimator (Davis & Peebles 1983) for our correlation measurements, so that

$$\xi^{rs}(r_p, r_\pi) = \frac{DD}{DR} - 1, \tag{2}$$

where DD and DR represent the number counts of pairs of two data galaxies, one data and one random galaxies, respectively. We have also computed w_p with the Landy-Szalay estimator (Landy & Szalay 1993) and the results are similar on all scales except above 30 h^{-1}Mpc, where the Landy-Szalay measurements show a slightly shallower slope than suggested by the matter clustering predicted by Planck on relevant scales. We have tested our analysis using the Landy-Szalay measurements and confirmed that the impact on our results are negligible.

As mentioned in § 1, the BOSS spectroscopic observation is subject to the fibre collision effect, so that galaxy pairs close to 62″ were severely under-sampled. Such effect can be partially remedied by sophisticated schemes that either takes advantage of the multiple passes of the survey (Guo et al. 2012), or the probabilistic distribution of close galaxies along the line of sight (Yang et al. 2019). However, those schemes were most intensively tested against a much denser sample (e.g., the SDSS Main Galaxy Sample), and it is unclear how robust the correction would work for BOSS. We therefore decide to apply the simplest nearest-neighbour correction and use distance scales above the fibre collision scale for our correlation function analysis. In particular, the maximum fibre-collided scale that corresponds to the maximum redshift of each of our four redshifts bins are 0.25 h^{-1}Mpc, 0.40 h^{-1}Mpc, 0.44 h^{-1}Mpc, 0.52 h^{-1}Mpc, respectively, and the minimum distance of our analysis is 0.6 h^{-1}Mpc across all redshift bins. For the g-g lensing signals, following Lange et al. (2019) we limit our fits to scales above 100 h^{-1}kpc, as on smaller scales the signals are strongly affected by the contributions from the galaxy stellar mass and the subhalo mass associated with the satellite galaxies (Zu & Mandelbaum 2015).

3 METHODOLOGY

We adopt an analytic HOD model to predict the number density distributions, projected auto-correlation functions, and g-g lensing signals of BOSS galaxies. Compared to studies using the simulation-based methods (Leauthaud et al. 2017; Guo et al. 2018), our method is computationally efficient when exploring the parameter space, but relatively lacking in accuracy, especially in the one-to-two-halo transition regime where the triaxial halo shape (Jing & Suto 2002) and halo exclusion becomes important (Tinker et al. 2005; Zu et al. 2014; García & Rozo 2019). Fortunately, our analysis is insensitive to the systematic uncertainties at the transition scales, as the statistical uncertainties of the current g-g lensing signals at those scales are similarly large (∼20−30%), and we primarily rely on the scales above (clustering) and below (lensing) for our constraints. However, we expect that an emulator-based method similar to that of (Wibking et al. 2019; Zhai et al. 2019; Nishimichi et al. 2019; Wibking et al. 2020) is necessary for exploring the cosmological information within the clustering and lensing of the BOSS galaxies and in future surveys.

The HOD model in our analysis was heavily based on the `iHOD` framework developed in a series of papers (Zu & Mandelbaum 2015, 2016), which drew insights from earlier works of Berlind & Weinberg (2002); Guzik & Seljak (2002); Tinker et al. (2005); Mandelbaum et al. (2006); Zheng & Weinberg (2007); Yoo et al. (2006); Leauthaud et al. (2011). We briefly describe the HOD prescription, with a focus on the modifications to the original `iHOD` framework, and refer the interested readers to the aforementioned two `iHOD` papers for details.

3.1 Halo Occupation Distribution

We start from the joint probability density distribution (PDF) of galaxy stellar mass M_* and host halo mass M_h,

$$p(M_*, M_h) = \frac{\lg e}{M_* n_g} \frac{\mathrm{d}N(M_*|M_h)}{\mathrm{d}\lg M_*} \frac{\mathrm{d}n}{\mathrm{d}M_h}, \quad (3)$$

where $\mathrm{d}N(M_*|M_h)/\mathrm{d}\lg M_*$ is the total number of galaxies (both observed and unobserved) per dex in stellar mass within halos at given mass M_h, n_g is the total galaxy number density, and $\mathrm{d}n/\mathrm{d}M_h$ is the halo mass function at Planck cosmology. Following Zu & Mandelbaum (2015), we hereafter refer to $\mathrm{d}N(M_*|M_h)/\mathrm{d}\lg M_*$ as $\langle N(M_*|M_h)\rangle$, assuming a fixed bin in logarithmic stellar mass.

The main advantage of starting with $p(M_*, M_h)$ is that, for an observed population of galaxies, whether it be quenched galaxies (Zu & Mandelbaum 2016) or BOSS observed galaxies as we study here, the 2D PDF of such population can be directly obtained by multiplying $p(M_*, M_h)$ and the 2D selection function $f_{\rm det}(M_*, M_h)$. In the case of studying galaxy quenching in Zu & Mandelbaum (2016), the 2D selection function is simply the 2D quenched fraction of galaxies as a function of M_* and M_h.

Our analytic model for $\langle N(M_*|M_h)\rangle$ has two components: 1) the mean and the scatter of the Stellar-to-Halo Mass Relation (SHMR) for the central galaxies, the combination of which automatically specifies $\langle N_{\rm cen}(M_*|M_h)\rangle$, and 2) the mean number of satellite galaxies with stellar mass M_* inside halos of mass M_h, $\langle N_{\rm sat}(M_*|M_h)\rangle$. We adopt the same parameterisation for the two components as in Zu & Mandelbaum (2015).

At fixed halo mass, we assume a log-normal probability distribution for the stellar mass of the central galaxies, hence a log-normal scatter. The mean SHMR is then the sliding mean of the log-normal distribution as a function of the halo mass, $f_{\rm SHMR} \equiv \exp\langle \ln M_*(M_h)\rangle$. We adopt a functional form for $f_{\rm SHMR}$ proposed by Behroozi et al. (2010) via its inverse function[1],

$$M_h = M_1 m^{\beta} 10^{(m^{\delta}/(1+m^{-\gamma})-1/2)}, \quad (4)$$

where $m \equiv M_*/M_{*,0}$. Among the five parameters that describe $f_{\rm SHMR}$, M_1 and $M_{*,0}$ are the characteristic halo mass and stellar mass that separate the behaviours in the low and high mass ends ($f_{\rm SHMR}(M_1) = \ln M_{*,0}$). The inverse function starts with a low-mass end slope β, crosses a transitional regime around $(M_{*,0}, M_1)$ dictated by γ, and reaches a high-mass end slope $\beta + \delta$. For the log-normal scatter, we keep the scatter independent of halo mass below M_1, but allow more freedom in the scatter above the characteristic mass scale, with an extra component that is linear in $\lg M_h$:

$$\sigma_{\ln M_*}(M_h) = \begin{cases} \sigma_{\ln M_*}, & M_h < M_1 \\ \sigma_{\ln M_*} + \eta \lg \frac{M_h}{M_1}, & M_h \geq M_1 \end{cases} \quad (5)$$

For the satellite populations, we model the expectation value of the satellite occupation $\langle N_{\rm sat}(M_*|M_h)\rangle$ as the derivative of the satellite occupation number in stellar mass-thresholded samples, $\langle N_{\rm sat}(> M_*|M_h)\rangle$, which is parameterised as a power of halo mass and scaled to $\langle N_{cen}(> M_*|M_h)\rangle$ as follows,

$$\langle N_{\rm sat}(> M_*|M_h)\rangle = \langle N_{\rm cen}(> M_*|M_h)\rangle \left(\frac{M_h}{M_{\rm sat}}\right)^{\alpha_{\rm sat}}. \quad (6)$$

We do not include the exponential cut-off in the equation 22 of Zu & Mandelbaum (2015), which has negligible impact on our constraints. We parameterise the characteristic mass of a single satellite-hosting halo $M_{\rm sat}$ as a simple power law function of the threshold stellar mass, so that

$$\frac{M_{\rm sat}}{10^{12}h^{-2}M_\odot} = B_{\rm sat}\left(\frac{f^{-1}_{\rm SHMR}(M_*)}{10^{12}h^{-2}M_\odot}\right)^{\beta_{\rm sat}}. \quad (7)$$

In practice, we choose a 0.02 dex bin size in stellar mass for the numerical differentiation of $\langle N_{\rm sat}(> M_*|M_h)\rangle$.

For any given sample defined between $M_*^{\rm min}$ and $M_*^{\rm max}$, the PDF of satellite occupation was commonly assumed to be Poisson with a mean of $\langle N_{\rm sat}(M_h)\rangle \equiv \langle N_{\rm sat}(M_*^{\rm min} < M_* < M_*^{\rm max}|M_h)\rangle$, so that the expected total number of satellite pairs within a halo of mass M_h is $\langle N_{\rm sat}(M_h)\,(N_{\rm sat}(M_h)-1)\rangle = \langle N_{\rm sat}(M_h)\rangle^2$ (Berlind & Weinberg 2002). However, in the BOSS sample we anticipate that the distribution of satellite occupation is narrower than Poisson: the underlying population of massive LRGs is more concentrated in the inner halo region than the average galaxies due to dynamical friction (Chandrasekhar 1943), but the fibre collision effect would remove many of the close pairs of LRGs to even out the observed satellite occupation numbers across halos of the same mass. We test this ansatz by measuring the number of close neighbours $N_{\rm close}$ around massive LRGs that are at least 50 per cent more massive than the second massive neighbour within a projected distance of $1\,h^{-1}$Mpc and a line-of-sight separation of $\Delta v = \pm 500\,{\rm km}/s$ (see "locally brightest galaxies" in Anderson et al. 2015; Mandelbaum et al. 2016). Among the systems with at least one close neighbour, $N_{\rm close}$ is predominantly unity, with a few per cent of them having $N_{\rm close} \geq 2$. Therefore, we adopt a satellite occupation distribution similar to the model "Average" described in Berlind & Weinberg (2002), so that if $\langle N_{\rm sat}(M_h)\rangle$ is between integers i and $j{=}i+1$, the halo has $p{=}\langle N_{\rm sat}(M_h)\rangle - i$ chance of hosting j satellites, and $1{-}p{=}j{-}\langle N_{\rm sat}(M_h)\rangle$ chance of hosting one fewer satellites. Therefore, the expectation number of satellite pairs within a halo of mass M_h is $2\,\langle N_{\rm sat}(M_h)\rangle\, i{-}ij$, substantially smaller than the Poisson expectation of $\langle N_{\rm sat}(M_h)\rangle^2$ when $\langle N_{\rm sat}(M_h)\rangle \leq 2$.

In order to model the spatial distribution of galaxies within halos, we assume the isotropic Navarro-Frenk-White (NFW: Navarro et al. 1997) density profile for halos with the concentration–mass relation $c_{\rm dm}(M_h)$ calibrated by Zhao et al. (2009). We place central galaxies at the barycentres of the NFW halos, and assume an NFW profile for the satellite distribution, but with a different amplitude of the concentration–mass relation than the dark matter. In particular, we set $c_{\rm sat}(M_h) \equiv f_c \times c_{\rm dm}(M_h)$, where f_c characterises the spatial distribution of satellite galaxies relative to the dark matter within halos.

Armed with the PDFs of the central and satellite occupations of each galaxy sample, we can predict the 3D real–space galaxy auto–correlation function ξ_{gg} and the galaxy–matter cross–correlation function ξ_{gm}, using the halo mass and bias functions predicted at the median redshift of the sample for the Planck 2020 cosmology. The technical details of this prediction can be found in Zu & Mandelbaum (2015). The signals of w_p and $\Delta\Sigma$ are then obtained by projecting ξ_{gg} and ξ_{gm} along the line of sight, respectively. The projection of ξ_{gg} to w_p is given by Equation (1), while for the g-g lensing it is via

$$\Delta\Sigma(r_p) = \langle\Sigma(< r_p)\rangle - \Sigma(r_p), \quad (8)$$

where

$$\Sigma(r_p) = \bar{\rho}_m \int_{-\infty}^{+\infty} \left[1 + \xi_{gm}(r_p, r_\pi)\right]\, \mathrm{d}r_\pi, \quad (9)$$

[1] There was a typo in the equation 19 of Zu & Mandelbaum (2015): exp → 10

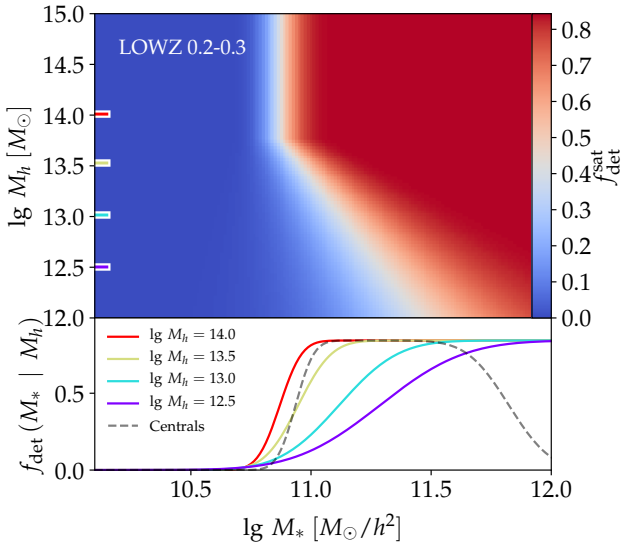

Figure 3. *Top*: The best-fitting 2D selection function of satellite galaxies in the LOWZ 0.2−0.3 sample on the lg M_* vs. lg M_h plane, colour-coded by the colour bar on the right. *Bottom*: The 1D satellite selection functions within haloes of four different masses (solid curves) and the central selection function predicted for the LOWZ 0.2−0.3 sample (gray dashed curve) as described by Equation 12. The LOWZ 0.2−0.3 sample preferentially selected satellite galaxies from the higher mass haloes below M_h=13.76.

and

$$\langle \Sigma(< r_p) \rangle = \frac{2}{r_p^2} \int_0^{r_p} r'_p \Sigma(r'_p)\, {\rm d}r'_p. \quad (10)$$

When computing the predictions for w_p, we apply a correction for the residual redshift-space distortion effect that causes an enhancement of w_p on large scales due to the non-zero pairwise velocity between galaxies separated beyond $r_\pi^{\rm max}$=100 h^{-1}Mpc, following the recipe of van den Bosch et al. (2013). Meanwhile for predicting $\Delta\Sigma$, we do not include the contributions from the galaxy stellar mass and the subhalo mass as was done in Zu & Mandelbaum (2015), because we have limited our fit to scales above 0.1 h^{-1}Mpc where these two terms are sub-dominant.

Finally, the galaxy SMF can be obtained simply as

$$\Phi(M_*) = n_g \int_0^{+\infty} p(M_*, M_h)\, f_{\rm det}(M_*, M_h)\, {\rm d}M_h, \quad (11)$$

where the 2D selection function $f_{\rm det}(M_*, M_h)$ will be modelled separately for centrals and satellites (as will be described in § 3.2).

To summarise the standard HOD prescription, we have 11 model parameters so far. Among them $\{\lg M_h^1, \lg M_*^0, \beta, \delta, \gamma\}$ describe the mean SHMR, $\{B_{\rm sat}, \beta_{\rm sat}, \alpha_{\rm sat}\}$ describe the parent HOD of satellite galaxies, $\{\sigma_{\ln M_*}, \eta\}$ describe the logarithmic scatter about the mean SHMR, and f_c is the ratio between the concentrations of the satellite distribution and the dark matter profile.

3.2 2D Selection Function of BOSS Galaxies

In the absence of any selection functions, the HOD prescription described in § 3.1 would be adequate for predicting the measured SMF, w_p, and $\Delta\Sigma$ for volume-limited stellar mass samples. As introduced in § 1 and § 2, the BOSS colour and magnitude cuts have introduced a complex selection function that we will model as a 2D function of M_* and M_h. Motivated by the findings in (Zu & Mandelbaum 2016), we model the central and satellite selection functions separately, as the quenched fractions of centrals vs. satellites exhibit different dependences on halo mass.

For the central galaxies, based on the findings in § 2.2 we conclude that the selection is largely independent on halo mass, so that the detection fraction can be reduced into a single-parameter function $f_{\rm det}^{\rm cen}(M_*)$. Informed by the measurements in Figure 2 and inspired by the functional form of Leauthaud et al. (2016), we model the central detection fraction as

$$f_{\rm det}^{\rm cen}(M_*) = \frac{f_{\rm max}}{2} \left(1 + {\rm erf}\left[(\lg M_* - \lg M_*^c)/\sigma^c\right]\right) f_{\rm cut}(M_*), \quad (12)$$

where $f_{\rm max}$ is the maximum detection fraction, $\lg M_*^c$ is the characteristic stellar mass at which $f_{\rm det}^{\rm cen}$ drops to $f_{\rm max}/2$, σ^c dictates the width of the decline into zero, and $f_{\rm cut}(\lg M_*)$ describes the cut-off at the high stellar mass end. For the LOWZ 0.2−0.3 sample, we fix the cut-off based on the Figure 2 results

$$f_{\rm cut}(M_*) = \frac{1}{2} \left(1 - {\rm erf}\left[(\lg M_* - 11.83)/0.194\right]\right), \quad (13)$$

while for the CMASS samples we set $f_{\rm cut}(M_*) = 1$.

At fixed stellar mass, the central galaxies reside in haloes within a narrow range of halo mass because of the small scatter in the SHMR (~0.2 dex). Therefore, it is unsurprising that the central selection function is insensitive to halo mass. However, the host haloes of the satellites usually have a much larger spread in halo mass, and the quenched fraction of satellites increases significantly with halo mass. Thus, we anticipate an extra halo mass dependence

Table 1. Posterior constraints of the model parameters for the four redshift samples. The uncertainties are the 68% confidence regions derived from the 1D posterior probability distributions.

Parameter	LOWZ 0.2−0.3	CMASS 0.43−0.51	CMASS 0.51−0.57	CMASS 0.57−0.70
$\lg M_h^1$	$13.00^{+0.29}_{-0.32}$	$13.08^{+0.27}_{-0.33}$	$13.35^{+0.13}_{-0.17}$	$13.41^{+0.22}_{-0.27}$
$\lg M_*^0$	$10.76^{+0.12}_{-0.13}$	$10.71^{+0.14}_{-0.20}$	$10.86^{+0.06}_{-0.07}$	$10.99^{+0.08}_{-0.11}$
δ	$0.38^{+0.05}_{-0.08}$	$0.85^{+0.17}_{-0.14}$	$1.19^{+0.19}_{-0.18}$	$1.10^{+0.23}_{-0.23}$
β	$0.74^{+0.19}_{-0.17}$	$0.71^{+0.17}_{-0.12}$	$0.72^{+0.17}_{-0.09}$	$0.80^{+0.18}_{-0.14}$
γ	$2.61^{+0.57}_{-0.59}$	$1.35^{+0.55}_{-0.56}$	$2.92^{+1.08}_{-0.94}$	$1.96^{+0.89}_{-0.84}$
$\sigma_{\ln M_*}$	$0.42^{+0.03}_{-0.03}$	$0.47^{+0.04}_{-0.04}$	$0.50^{+0.04}_{-0.03}$	$0.49^{+0.04}_{-0.04}$
η	$0.01^{+0.01}_{-0.01}$	$0.39^{+0.09}_{-0.08}$	$0.48^{+0.14}_{-0.12}$	$0.26^{+0.11}_{-0.08}$
$B_{\rm sat}$	$5.53^{+2.08}_{-1.66}$	$5.62^{+2.34}_{-1.92}$	$3.60^{+1.57}_{-1.30}$	$9.32^{+3.87}_{-3.28}$
$\beta_{\rm sat}$	$0.94^{+0.11}_{-0.09}$	$0.36^{+0.11}_{-0.10}$	$0.24^{+0.06}_{-0.05}$	$0.24^{+0.09}_{-0.08}$
f_c	$0.38^{+0.26}_{-0.18}$	$0.68^{+0.32}_{-0.27}$	$3.38^{+1.58}_{-1.29}$	$1.13^{+0.55}_{-0.48}$
$\alpha_{\rm sat}$	$1.00^{+0.03}_{-0.03}$	$0.99^{+0.03}_{-0.04}$	$0.97^{+0.03}_{-0.03}$	$0.99^{+0.03}_{-0.03}$
$\lg M_*^c$	$10.94^{+0.01}_{-0.01}$	$10.96^{+0.09}_{-0.07}$	$11.25^{+0.22}_{-0.15}$	$11.44^{+0.17}_{-0.12}$
σ^c	$0.09^{+0.01}_{-0.01}$	$0.21^{+0.05}_{-0.05}$	$0.27^{+0.09}_{-0.08}$	$0.42^{+0.07}_{-0.07}$
μ	$-0.33^{+0.11}_{-0.13}$	$0.24^{+0.07}_{-0.06}$	$0.38^{+0.08}_{-0.07}$	$0.36^{+0.10}_{-0.09}$
ν	$-0.23^{+0.06}_{-0.06}$	$0.30^{+0.08}_{-0.06}$	$0.35^{+0.06}_{-0.05}$	$0.35^{+0.09}_{-0.07}$
$\lg M_*^s$	$10.88^{+0.03}_{-0.03}$	$11.39^{+0.19}_{-0.17}$	$11.96^{+0.28}_{-0.28}$	$11.86^{+0.28}_{-0.25}$
$\lg M_h^s$	$13.76^{+0.28}_{-0.24}$	$15.01^{+0.59}_{-0.33}$	$15.44^{+0.76}_{-0.48}$	$14.87^{+0.70}_{-0.48}$
σ^s	$0.10^{+0.02}_{-0.02}$	$0.76^{+0.16}_{-0.13}$	$1.09^{+0.25}_{-0.19}$	$1.00^{+0.24}_{-0.20}$
$f_{\rm max}$	$0.84^{+0.06}_{-0.05}$	$0.84^{+0.05}_{-0.05}$	$0.86^{+0.06}_{-0.06}$	$0.86^{+0.06}_{-0.05}$

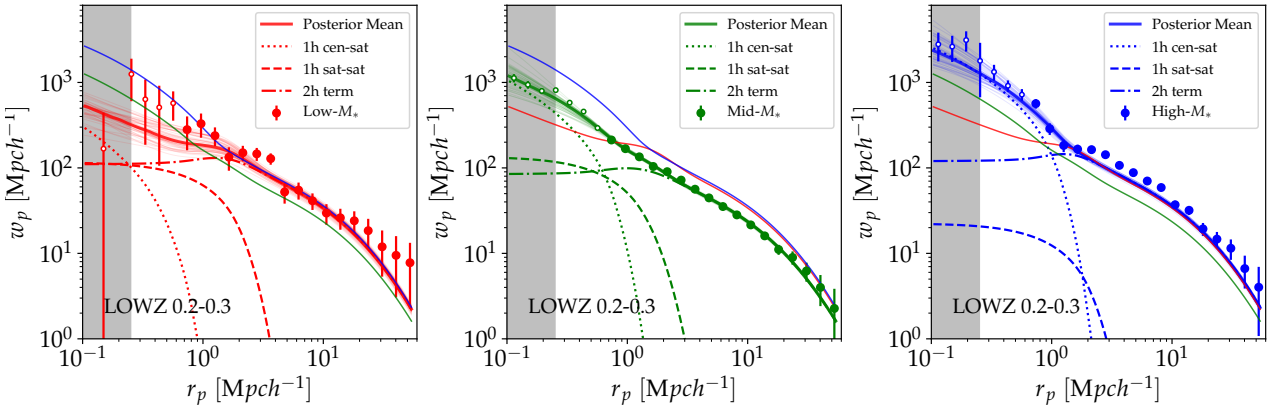

Figure 4. Comparison between the projected auto-correlation functions w_p measured from data and predicted from the posterior mean model, for the Low−M_* (left), Mid−M_* (middle), and High−M_* (middle) stellar mass subsamples of the LOWZ 0.2−0.3 galaxies. In each panel, large filled circles with errorbars are the measurements used by our analysis, while the small open circles below $0.6\,h^{-1}$Mpc are left unused by our model fit due to the potential impact from fibre collision. The vertical shaded region represents the distance scales that are below the maximum fibre-collided distance scale at the maximum redshift of the sample (z=0.3). Thick solid curve is the posterior mean prediction from our MCMC analysis, with the thin bundle of curves of the same colour showing the predictions from 100 random steps along the MCMC chain. The two other solid curves with different colours (but consistent across the three panels) indicate the posterior mean predictions for the other two stellar mass subsamples. Dotted and dashed lines indicate the contributions from the central-satellite pairs and satellite-satellite pairs within the same halo, respectively. Dot-dashed line indicates the contribution from the galaxy pairs between different haloes.

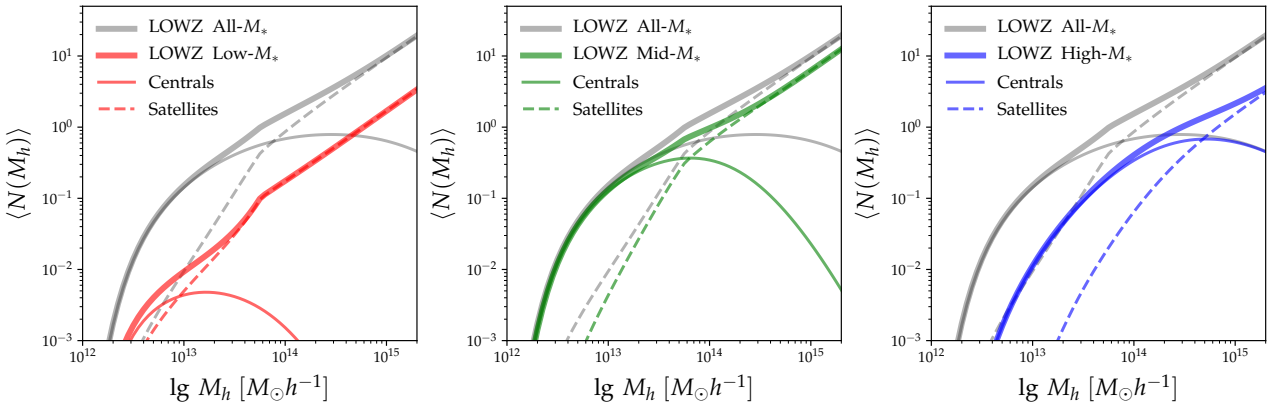

Figure 5. HODs predicted by the best-fitting model for the Low-M_* (left), Mid-M_* (middle), High-M_* (right) subsamples in the LOWZ 0.2−0.3 sample. In each panel, the red, green, or blue curves describe the set of HODs for the stellar mass subsample, while the gray curves are for the entire LOWZ 0.2−0.3 sample (same across all three panels). For each set of HODs, thin solid and thin dashed curves indicate the HODs of the central and satellite galaxies, respectively, and the sum of the two are shown as the thick solid curve.

in the satellite selection function of the BOSS samples,

$$f_{\rm det}^{\rm sat}(M_*) = \frac{f_{\rm max}}{2}\left(1+{\rm erf}\left[\left(\lg M_* - \lg M_*^s(M_h)\right)/\sigma^s(M_h)\right]\right), \tag{14}$$

where

$$\lg M_*^s(M_h) = \begin{cases} \lg M_*^s + \mu(\lg M_h - \lg M_h^s), & M_h < M_h^s \\ \lg M_*^s, & M_h \geq M_h^s, \end{cases} \tag{15}$$

and

$$\sigma^s(M_h) = \begin{cases} \sigma^s + \nu(\lg M_h - \lg M_h^s), & M_h < M_h^s \\ \sigma^s, & M_h \geq M_h^s, \end{cases} \tag{16}$$

respectively. In Equations 15 and 16, M_h^s is a characteristic halo mass beyond which the satellite selection function depends only on stellar mass, and μ and ν dictate the variation of the characteristic stellar mass and transition width with halo mass below M_h^s, respectively. We assume the same $f_{\rm max}$ for centrals and satellites during the fit as it is likely independent of galaxy properties. Therefore, the satellite detection fraction at fixed halo mass has a similar form compared to the central detection fraction (without the high mass cut-off), but both the characteristic stellar mass and the transition width vary with halo mass below M_h^s. The halo-mass independence above M_h^s is intended to mimic the fact that the satellite colours have converged to the red-sequence in the most massive systems. Below M_h^s, non-zero values of μ and ν would select galaxies with different stellar mass distributions into the BOSS sample.

Figure 3 illustrates the 2D satellite selection function (top panel) and the 1D satellite (coloured curves in the bottom panel) vs. central selection functions (gray dashed curve in the bottom panel), respectively, predicted by the best-fitting model for the LOWZ 0.2−0.3 sample (as will be described later in § 4). The

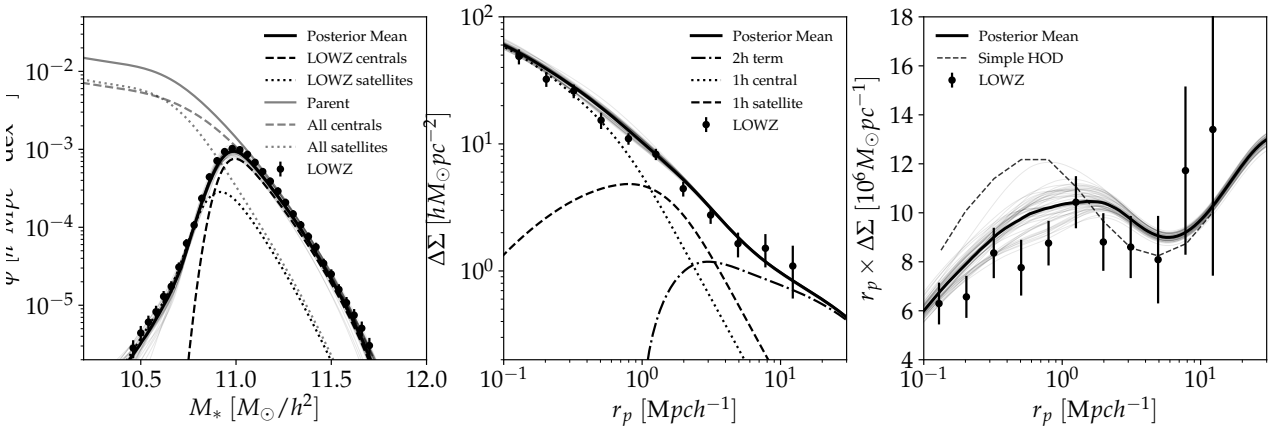

Figure 6. *Left*: Comparison between the observed (data points with errorbars) and posterior mean predicted (thick solid curve) SMFs for the LOWZ 0.2−0.3 sample. The bundle of thin solid curves surrounding the thick solid curve indicates the predictions from 100 random steps along the MCMC chain, while the dashed and dotted black curves represent the contributions from the central and satellite galaxies, respectively. Gray solid, dashed, and dotted curves are the SMFs of the stellar mass-complete sample predicted by the posterior mean model. *Middle*: Comparison between the observed (data points with errorbars) and posterior mean predicted (thick solid curve) g-g lensing signals. The thin bundle of curves are the predictions from 100 random MCMC steps. Dotted, dashed, and dot-dashed curves are the contributions from the one-halo central, one-halo satellite, and two-halo lensing terms, respectively. *Right*: Similar to the middle panel, but with the y-axis replaced by $r_p \times \Delta\Sigma$. Dashed curve shows the prediction from the model derived from clustering in Lange et al. (2019). The posterior mean prediction from our model successfully reproduces the observed SMF and g-g lensing signal on all scales.

2D satellite selection map indicates that the selection function depends only on stellar mass at M_h>13.76, but diverges into a wider transition and higher stellar mass threshold with decreasing halo mass. Compared to the central selection function (gray dashed), the 1D satellite selection functions have similarly sharp transitions and characteristic stellar mass at high M_h, but selects significant lower fraction of galaxies at high stellar mass from low mass haloes.

To summarise the selection function prescription, we have eight model parameters. Among them $\{\lg M_*^c, \sigma^c\}$ describe the selection function of centrals galaxies, $\{\lg M_h^s, \lg M_*^s, \sigma^s, \mu, \nu\}$ describe the 2D selection function of satellite galaxies, and $f_{\rm max}$ is the maximum detection fraction of the sample.

Finally, combining the HOD (§ 3.1) and selection function (§ 3.2) prescriptions, our model has 19 parameters. Note that we have employed the full HOD prescription from Zu & Mandelbaum (2015), which was designed to fit all the galaxies above $\lg M_*$=8.5, while our minimum stellar mass is approximately two orders of magnitudes higher at $\lg M_*$=10.5. As a result, most of the parameters that describe the low-mass end behaviours will be prior-dominated. Furthermore, the investigation of redMaPPer BCGs in § 2.2 has greatly reduced the number of parameters for the central galaxy selection modelling compared to the satellites.

3.3 Gaussian Likelihood Model

Equipped with the capability of predicting the SMF $\phi(M_*)$, projected auto-correlation function $w_p(r_p)$, and g-g lensing signals $\Delta\Sigma(r_p)$ for each of the four BOSS samples, we can infer the posterior probability distribution of the model parameters from fitting the three observables within a Bayesian framework assuming a Gaussian likelihood model.

We include two components in the error matrices of the observed SMFs, one is the Poisson errors from number counting, the other is an extra term representing the sample variance and uncertainties in the comoving volume calculation due to the uncertainties in cosmology and effective area. For the second term, we add an additional 10 per cent error in the diagonal term with a 50 per cent covariance in the off-diagonal terms. The error matrices of w_p is directly estimated from the data using the jackknife re-sampling technique, by dividing the LOWZ/CMASS northern sky coverage into 200 patches of the similar area. We adopt the same error matrices of the g-g lensing signals from Lange et al. (2019) and Leauthaud et al. (2017) for LOWZ and CMASS galaxies, respectively. When combining the three observables into one data vector, we ignore the weak covariance among the three types of observables, and among the different stellar mass subsamples of the same redshift bin.

We model the combinatorial vector $\mathbf{x}$ of ϕ, w_p, and $\Delta\Sigma$ as a multivariate Gaussian, which is fully specified by its mean ($\bar{\mathbf{x}}$) and covariance matrix ($\mathbf{C}$). The Gaussian likelihood is thus

$$\mathcal{L}(\mathbf{x}|\boldsymbol{\theta}) = |\mathbf{C}|^{-1/2} \exp\left(-\frac{(\mathbf{x}-\bar{\mathbf{x}})^T \mathbf{C}^{-1} (\mathbf{x}-\bar{\mathbf{x}})}{2}\right), \quad (17)$$

where

$$\boldsymbol{\theta} \equiv \{\lg M_h^1, \lg M_*^0, \beta, \delta, \gamma, B_{\rm sat}, \beta_{\rm sat}, \alpha_{\rm sat}, \sigma_{\ln M_*}, \eta, f_c, \lg M_*^c, \sigma^c, \lg M_h^s, \lg M_*^s, \sigma^s, \mu, \nu, f_{\rm max}\}. \quad (18)$$

To focus our constraint on the stellar mass range above $\lg M_*$>10.5, we place priors on both the slope and scatter of the SHMR at the low-mass end. In particular, we limit the predicted mean stellar mass at halo mass $10^{11}\ h^{-1}M_\odot$ to be between $10^8 h^{-2} M_\odot$ and $10^9 h^{-2} M_\odot$, informed by the study of the SHMR evolution with redshift in Yang et al. (2012). We also place a Gaussian prior on $\sigma_{\ln M_*} \sim \mathcal{N}(0.50, 0.04^2)$, informed by the constraints from Zu & Mandelbaum (2015). The slope prior is not directly applied on any of the parameters because our SHMR parameterization does not allow a clean separation of the low and high-mass end slopes, which is however possible in other parameterisations(e.g., Yang et al. 2012). Finally we place a Gaussian prior on $f_{\rm max} \sim \mathcal{N}(0.86, 0.05^2)$, informed by our direct measurement from § 2.2.

For each redshift bin, the joint posterior distribution of the parameters is derived using the Markov Chain Monte Carlo (MCMC)

algorithm `emcee` (Foreman-Mackey et al. 2013), where an affine-invariant ensemble sampler is utilised to fully explore the parameter space. For each MCMC chain, we perform 40, 0000 iterations, 100, 000 of which belong to the burn-in period for adaptively tuning the steps. To eliminate the residual correlation between adjacent iterations, we further thin the chain by a factor of 10 to obtain our final results. The 68 per cent confidence regions of the 1D posterior constraints are listed in Table 1, with one column for each of four redshift bins.

4 RESULTS FROM LOWZ

We highlight the results from our joint analysis of the Φ, w_p, and $\Delta\Sigma$ for the LOWZ 0.2−0.3 sample in this Section, starting by examining the model fits to the w_p measurements of the three stellar mass bins below. Compared to Lange et al. (2019) analysis, we employ the same g-g lensing signals measured by their work, but divide the LOWZ galaxies into three stellar mass subsamples, each of which covers a distinctive portion of the observed SMF, rather than two (arbitrary) subsamples of equal logarithmic bin width. The deliberate stellar mass binning helps elicit the important information on the dependence of large-scale bias on stellar mass, and more important, satellite fraction.

Figure 4 compares the measured projected auto-correlation functions to predictions from our posterior mean model for the three stellar-mass bins in the LOWZ 0.2−0.3 sample (stellar mass increases from left to right). In each panel, circles with errorbars show the w_p measurements for the particular stellar mass bin, with large solid circles indicating the data points used for the model fit and small open ones the data points unused due to fibre collision. The vertical shaded region on the left of each panel indicates the scales below the maximum comoving distance that the fibre radius corresponds to at z=0.3, which is well below the 0.6 h^{-1}Mpc minimum fitting scale that separates the large solid and small open circles. The posterior mean prediction from our model is indicated by the thick solid curve, with the bundle of thin curves of the same colour indicating the predictions from 100 random steps along the MCMC chain. For the sake of straight comparison of the three stellar mass bins, we also show the respective posterior mean predictions for the other two stellar mass bins as the two solid lines of different colours (but consistent with the colours in their respective panels). Under the solid curves, the dotted and dashed curves indicate the contributions from the one-halo central-satellite and the one-halo satellite-satellite terms to the overall predicted signal, respectively, while the dot-dashed curve indicates the two-halo term.

On large scales, the w_p signal has a non-monotonic dependence on stellar mass, with the Mid-M_* subsample (green) showing the lowest galaxy bias than the Low-M_* and High-M_* subsamples which show comparable clustering amplitudes to each other. Such non-monotonic behavior of galaxy bias is well described by the model predictions. The shape of the measured w_p of the Low-M_* bin shows a deviation from that of a biased matter clustering on scales larger than $20h^{-1}$Mpc, but is still consistent with model prediction within the large errorbars. Meanwhile, the measured w_p of the High-M_* bin exhibits a flattening feature at $r_p \simeq 2h^{-1}$Mpc, followed an enhancement compared to the prediction on scales between $3-5h^{-1}$Mpc. Since the galaxies in the high mass bin are dominated by the central galaxies of massive haloes, this feature is likely associated with the galaxy kinematics and distribution in the infall region, which may require specially-tailored models like those in Zu & Weinberg (2013). On small scales, the clustering is subject to the fibre collision effect, but the model predictions agree reasonably well with the small open circles that are above the maximum fibre radius (i.e., outside of the gray shaded region). This agreement, combined the fact that we do not see a sudden decrease in the clustering amplitude, suggests that the impact from fibre collision is weak in the LOWZ 0.2−0.3 sample.

To understand the behaviors of the measured and predicted w_p signals, we examine the HOD of each of three subsamples in Figure 5 (stellar mass increases from left to right). In each panel, we show the HODs of the entire LOWZ 0.2−0.3 sample in gray as the reference HOD, and the results of the stellar mass subsample in one of red (Low-M_*), green (Mid-M_*), or blue (High-M_*) colours. For each sample, we show the HODs of the central and satellite galaxies as thin solid and thin dashed curves, respectively, and the sum of the two in thick solid curve. As expected, the Low-M_* subsample is dominated by satellite galaxies in massive haloes, while the High-M_* subsample consists mainly of central galaxies in haloes of similar mass. Therefore, although the average stellar mass of those two subsamples are different by ∼0.5 dex, they exhibit almost the same large-scale galaxy bias. The satellite HOD of the Low-M_* subsample (red dashed curve in left panel) shows a kink at lg M_h=13.76, where the satellite selection function starts to depend on halo mass, thereby showing a steeper slope than at the high-M_h end (∼1). Clearly, this kink is directly related to the deflection of the half-$f_{\rm max}$ track (delineated by the white colour) on the satellite detection map in Figure 3.

In the middle panel of Figure 5, the HOD of the Mid-M_* subsample is dominated by the central galaxies in group-size haloes, hence the lower large-scale bias than the other two, which reflect the bias of cluster-size haloes. We emphasize again that, since the HOD of the total LOWZ 0.2−0.3 sample is dominated by the Mid-M_* subsample at the peak of the observed SMF, fitting to the w_p measurements of the total sample alone would not provide the key information on the halo mass dependence of the satellite selection function revealed by the Low-M_* and High-M_* subsamples.

Given that the HODs displayed in Figure 5 provide excellent description to the nontrivial stellar mass dependence of galaxy clustering on both small and large scales, it is intriguing whether it could also reproduce the observed SMF, and most importantly, the g-g lensing signals. We first compare the observed and posterior mean SMFs in the left panel of Figure 6, where data points with errorbars are the measured SMF and thick solid curve is our posterior mean prediction, with the thin bundle of curves showing predictions from 100 random steps along the MCMC chain. Underneath the thick solid curve we decompose the predicted SMF into contributions from the central (black dashed) and satellite (black dotted) galaxies. The gray solid, dashed, and dotted curves are the predicted total, central, and satellite SMFs of the parent LOWZ 0.2−0.3 sample (i.e., 100 per cent completeness). The posterior mean SMF provides an excellent description of the observed stellar mass distribution of LOWZ 0.2−0.3 galaxies, including the slope change at the low mass end. As expected from our intuition in § 2.1, the central SMF has a sharp cutoff at lg M_*=10.94, vacating the low stellar mass portion to satellite galaxies. The slope change at lg M_*=10.7 is the direct consequence of preferentially selecting galaxies at the low stellar mass tail from massive halos. One useful test of our model is to compare the predicted parent SMF (thin solid curve) to those inferred from multi-band deep imaging data by, e.g, Leauthaud et al. (2016); Unfortunately the large discrepancy in the stellar mass estimates from spectroscopy vs. imaging makes such direct comparison difficult (see figure 15 in their paper).

Finally, we examine the g-g lensing signals in the middle and

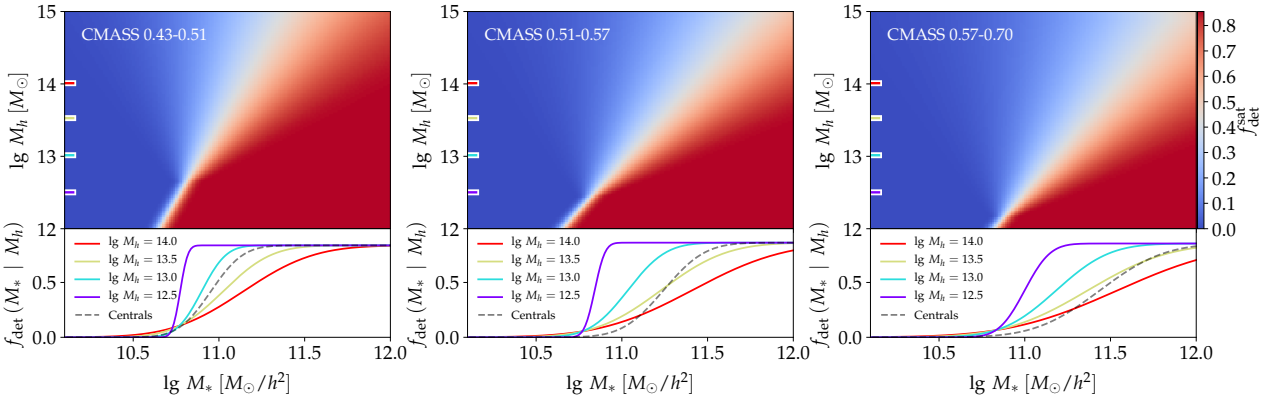

Figure 7. Similar to Figure 3, but for CMASS 0.43−0.51 (left), CMASS 0.51−0.57 (middle), and CMASS 0.57−0.70 (right), respectively. The selection function in CMASS preferentially observes satellite galaxies from low-mass haloes, compared to LOWZ which selects more satellites from high-mass haloes.

right panels of Figure 5. In both panels, data points with errorbars are the measurements for the entire LOWZ 0.2−0.3 sample, and thick solid curves are the posterior mean prediction from our model, with the thin bundle of curves indicating the individual predictions by 100 random steps along the MCMC chain. We multiply $\Delta\Sigma$ by r_p in the right panel to facilitate signal comparison across small and large scales. In the middle panel of Figure 5, we also show the decomposition into host halo lensing signal around centrals (dotted), host halo lensing signal around satellites (dashed), and the large-scale lensing signal from other neighbouring haloes (dot-dashed). The posterior model prediction provides an excellent fit to the g-g lensing measurements on all scales, without any strong lensing discrepancy on small scales. In the right panel of Figure 5, we additionally show the prediction from the best-fitting conditional stellar mass function model of Lange et al. (2019) (thin dashed curve), which does a slightly better job than our model on scales larger than $2h^{-1}$Mpc. However, the dashed curve significantly over-predicts the lensing signal on scales below $1h^{-1}$Mpc compared to the data points and to our posterior mean prediction.

To summarise, our best-fitting model successfully reproduces the observed SMF, galaxy clustering, and g-g lensing signals simultaneously at the Planck cosmology. The carefully binning in the stellar mass allows us a better constraint of satellite fraction $f_{\rm sat}$, which is signifiantly non-zero at the low stellar mass end. Meanwhile, the model allows the selection function of satellite galaxies to have an extra halo mass dependence, which breaks the lockstep between the small-scale lensing and large-scale galaxy bias that are only valid in the limit of $f_{\rm sat}\to 0$.

5 RESULTS FROM CMASS

In the previous Section we demonstrate that our model is capable of fully resolving the discrepancy between the large-scale clustering and small-scale lensing of the LOWZ 0.2−0.3 sample at Planck cosmology. We now move on to the three CMASS samples in which the original "lensing is low" discrepancy was discovered by Leauthaud et al. (2017). We apply our HOD analysis to the CMASS 0.43−0.51, CMASS 0.51−0.57, and CMASS 0.57−0.70 samples separately with the same set-up as in LOWZ 0.2−0.3. Since the constraints from the three samples are qualitatively similar, we will describe their results simultaneously below.

Figure 7 shows the galaxy selection functions predicted by the best-fitting models for CMASS 0.43−0.51 (left), CMASS 0.51−0.57 (middle), CMASS 0.57−0.70 (right), respectively. The format of each panel is the same as Figure 3. Compared to the results from LOWZ 0.2−0.3, the CMASS satellite selection functions inferred by the model exhibit a preference of selecting satellite galaxies from the *low-mass* haloes, rather than *high-mass* haloes as shown in Figure 3. This change of preference is likely caused by the combination of two factors, one observational and the other physical. Firstly, the CMASS colour selection includes more galaxies that are in the blue cloud, while the LOWZ selection follows more faithfully the traditional LRG colour cuts (Eisenstein et al. 2001). Secondly, galaxies in massive haloes are in general bluer at higher redshifts (Cooper et al. 2007; Hansen et al. 2009; Nishizawa et al. 2018). In addition, Figure 7 shows that this preference becomes even stronger for CMASS galaxies at higher redshifts, bringing relatively more galaxies from the low-mass haloes into the sample. This redshift dependence is consistent with the findings in Montero-Dorta et al. (2016), who estimated that the fraction of intrinsically blue galaxies in CMASS increases from ∼36 per cent at z=0.5 to ∼46 per cent at z=0.7 — satellite galaxies from lower-mass haloes are generally bluer.

Figure 8 compares the projected auto-correlation functions between the measurements and posterior mean predictions, for the CMASS 0.43−0.51 (top row), CMASS 0.51−0.57 (center row), and CMASS 0.57−0.70 (bottom row), respectively. The format of each row is the same as Figure 4, with the Low-M_*, Mid-M_*, and High-M_* results shown by the left, middle, and right panels, respectively. The most important difference among the three stellar mass subsamples is the stellar mass trend of the w_p signal on large scales. While the Mid-M_* and High-M_* signals show consistent trends across different redshifts, the relative bias of Low-M_* galaxies decreases as a function of redshift. However, even in the CMASS 0.43−0.51 subsample where the bias of the Low-M_* galaxies is the highest, it is still substantially lower than that of the High-M_* ones, unlike the case in LOWZ 0.2−0.3 where they are comparable. On small scales, the impact of fibre collision is clearly seen among the small open circles, which always experience a sudden drop entering the gray shaded region, i.e., the fiber-collided scales. Beyond the shaded region, However, the small open circles are largely consistent with our predictions, despite that those data points were never used for the model fit. Interestingly, for the Low-M_* subsamples, the model predictions agree well with the measured w_p even inside the fibre-collided regime. One possibility is that the Low-M_* subsamples

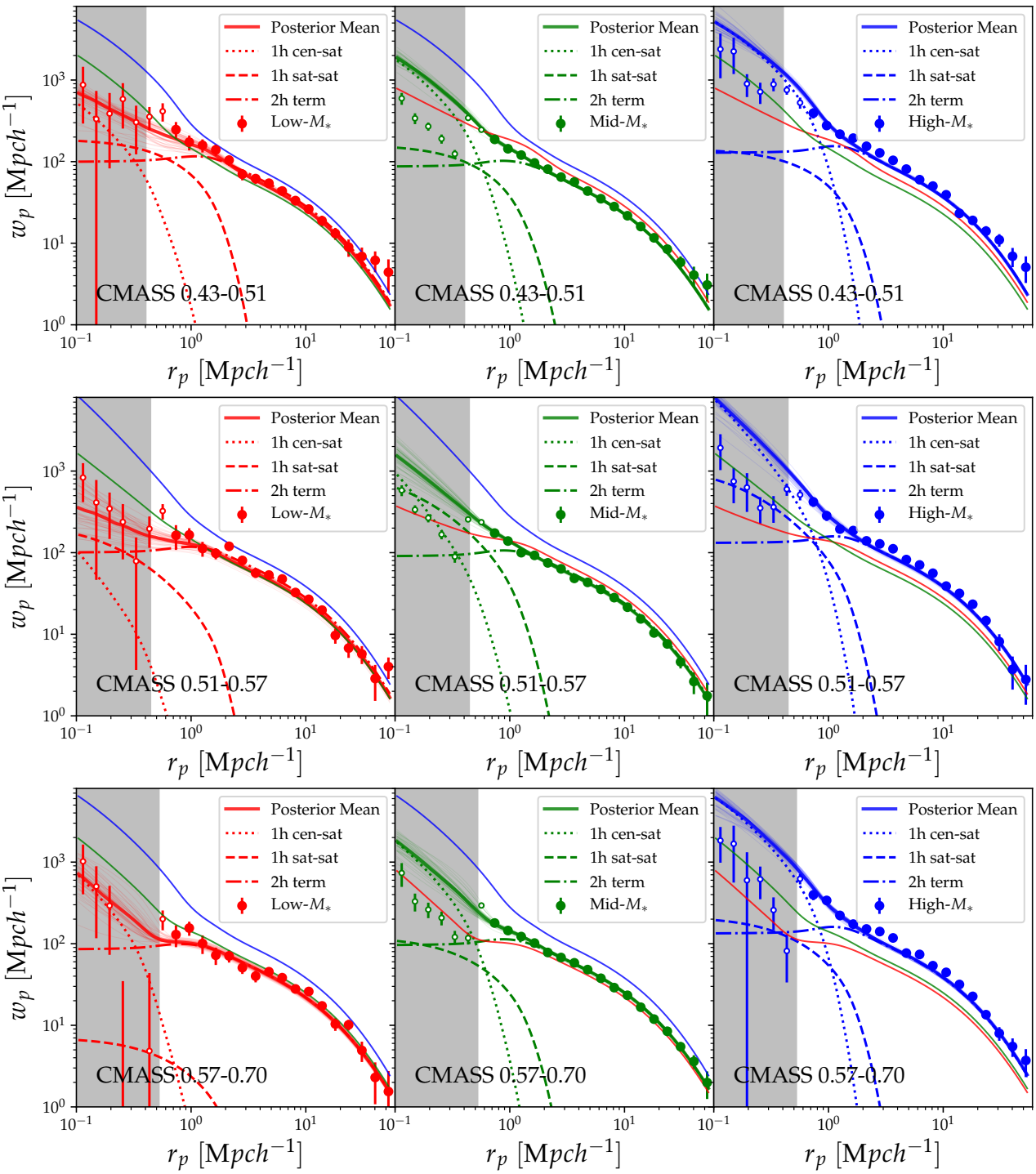

Figure 8. Similar to Figure 4, but for the CMASS 0.43−0.51 (top row), CMASS 0.51−0.57 (center row), and CMASS 0.57−0.70 (bottom row) subsamples, respectively.

consist mostly satellite galaxies without a dominant central in the nearby sky, hence a lower fibre collision probability.

The behaviours of the measured and predicted w_p signals can be understood by examining their HODs in Figure 9. The format of the Figure is similar to that of Figure 5, but we display the results for the three stellar mass subsamples in one panel instead of showing them separately. Overall, the stellar mass dependence of the HODs at each redshift is similar to one another. In general, the satellite HODs of the Low-M_* (red dashed curves) subsamples exhibit an enhancement at the low halo mass due to the preferential selection seen in Figure 7, which also helps bring down the relative galaxy bias of the CMASS Low-M_* subsamples compared to that in LOWZ.

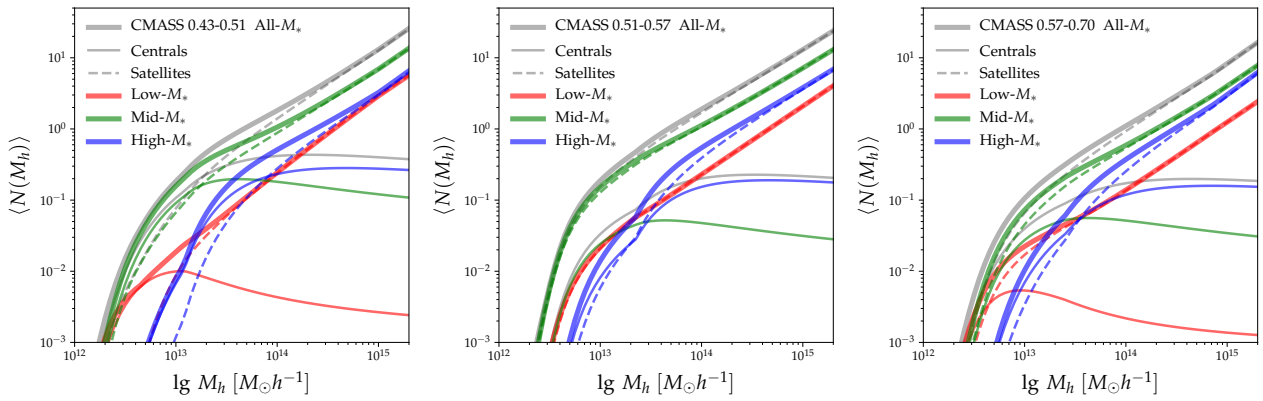

Figure 9. Similar to Figure 5, but for the CMASS 0.43−0.51 (left), CMASS 0.51−0.57 (middle), and CMASS 0.57−0.70 (right) subsamples, respectively. Instead of showing the three stellar mass subsamples in separate panels as in Figure 5, we display them in the same panel for each redshift bin, with Low-M_*, Mid-M_*, and High-M_* HODs shown in red, green and blue, respectively. Gray curves are the HODs of the overall sample.

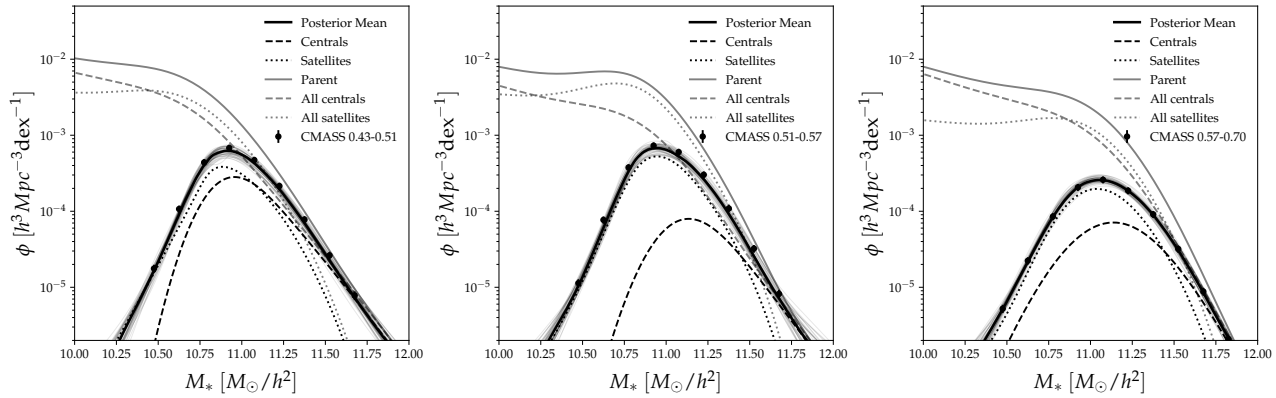

Figure 10. Similar to the left panel of Figure 6, but for the CMASS 0.43−0.51 (left), CMASS 0.51−0.57 (middle), and CMASS 0.57−0.70 (right) subsamples, respectively.

Intriguingly, the Low-M_* subsample of the CMASS 0.51−0.57 bin barely has any central galaxies. This is likely driven by the relatively low lensing amplitude on small scales (middle panels of Figure 11), as its impact on w_p is negligible.

We compare the observed SMFs to those predicted by our inferred HODs in Figure 10. The format of each panel is the same as in the left panel of Figure 6. Unlike the LOWZ 0.2−0.3 sample, there does not appear any feature on the observed CMASS SMFs (data points with errorbars), so the SMFs are less constraining compared to that in Figure 6. Nevertheless, we obtain excellent fits to the data with the same HODs that reproduce the clustering measurements. Therefore, the best-fitting HODs provide an excellent description of the joint redshift and stellar mass dependences of the clustering and abundance for CMASS galaxies.

We now examine the g-g lensing signals predicted by the best-fitting HODs, and compare if they remain systematically higher than observations on small scales. Figure 11 shows a comprehensive comparison between the observed g-g lensing signals (data points withe errorbars) and our posterior mean predictions (thick solid curves surrounded by a bundle of thin solid curves), for the CMASS 0.43−0.51 (left panels), CMASS 0.51−0.57 (middle panels), and CMASS 0.57−0.70 (right panels), respectively. In the top panels, we decompose the predictions into one-halo central (dotted), one-halo satellite (dashed) and two-halo (dot-dashed) terms. Meanwhile in the bottom panels, we highlight the comparison by showing $r_p \times \Delta\Sigma$ as the y-axis, and add two extra curves predicted by the Saito et al. (2016) (magenta solid) and Rodríguez-Torres et al. (2016) (blue dashed) analyses, both of which exhibit very strong lensing discrepancy on small scales. The Saito et al. (2016) predictions show similar large-scale lensing amplitudes to our curves, but on small scales are higher than the measurements by ∼40% in all three redshift bins. The Rodríguez-Torres et al. (2016) results show better agreement with the data for the CMASS 0.43−0.51 sample on scales above $0.3h^{-1}$Mpc compared to our curve, but significantly over-predict the signal on all scales for the other two samples, reaching a discrepancy as large as 50% for the CMASS 0.57−0.70 sample on small scales.

On scales above $1h^{-1}$Mpc, our predictions are in general higher than the observations by ∼30 per cent, except for the High-M_* subsample. This is slightly concerning — the large-scale lensing signal is fully determined by the galaxy bias at fixed cosmology, which is then tightly constrained by the projected clustering shown in Figure 8. Therefore, within our model framework at best-fitting Planck cosmology, it is very difficult to lower the large-scale lensing amplitude to be better matched to the measurements. In terms of uncertainties in the lensing signals, Leauthaud et al. (2017) did a

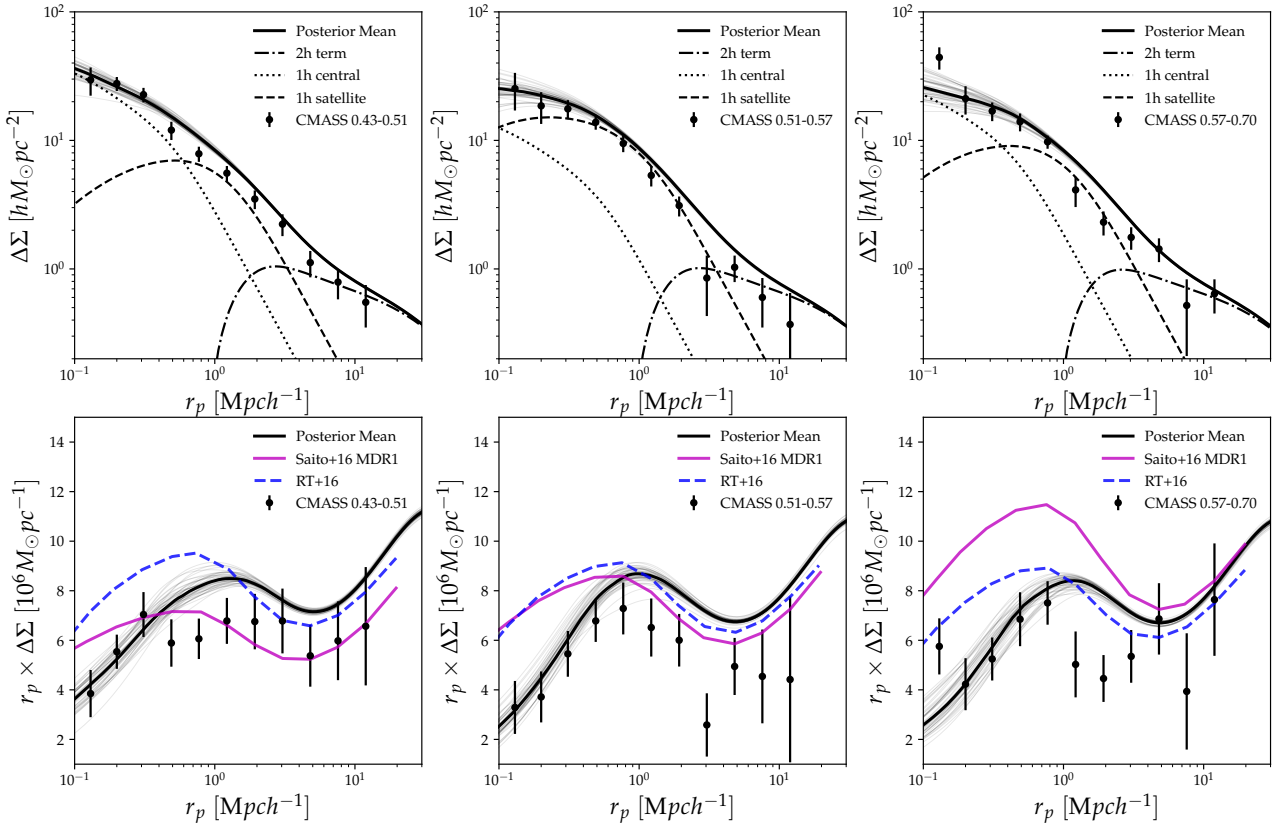

Figure 11. *Top*: Comparison between the measured g-g lensing signals (data points with errorbars) and the posterior mean predictions (thick solid curves surrounded by thin bundle of gray curves) from our model, for the CMASS 0.43−0.51 (left), CMASS 0.51−0.57 (middle), and CMASS 0.57−0.70 (right), respectively. Each thick solid curve is decomposed into contributions from the one-halo central (dotted), one-halo satellite (dashed), and two-halo terms, respectively. *Bottom*: Similar to the top panels, but with the y-axis changed to $r_p \times \Delta\Sigma$. In each panel, magenta solid and blue dashed curves are predictions that exhibit the original "lensing is low" discrepancy, from Saito et al. (2016) and Rodríguez-Torres et al. (2016), respectively. Our posterior model predictions provide an excellent description to the g-g lensing measurements on small scales below $1\,h^{-1}$Mpc, and a comparable fit to the large scales compared to the other two models.

comprehensive analysis of the possible sources of systematic errors, and concluded that the total fractional systematic error on $\Delta\Sigma$ is 5−10 per cent, much smaller than the large-scale discrepancy we see in Figure 11.

On scales below $1h^{-1}$Mpc, however, our predicted signals are in excellent agreement with the measurements, without showing any symptoms of a low lensing amplitude. This is very encouraging, indicating that the CMASS lensing discrepancy on small scales is also resolved, similar to that in our LOWZ 0.2−0.3 analysis. As pointed out by Leauthaud et al. (2017) and emphasized in § 1, the essence of the "lensing is low" discrepancy lies in the one-halo regime, where the observed small-scale lensing signal is lower than that inferred from the large-scale galaxy bias. Therefore, given that our model has provided excellent fits to the comprehensive galaxy clustering in Figure 8 and the small-scale g-g lensing in Figure 8, the original "lensing is low" discrepancy revealed by the CMASS galaxies is also reasonably resolved by our HOD model via the incorporation of a halo mass dependence in satellite selection.

6 CONCLUSION

In this paper, we have applied an analytic model based on the `iHOD` framework of Zu & Mandelbaum (2015, 2016), to the observed stellar mass functions ϕ, projected auto-correlation functions w_p, and g-g lensing signals $\Delta\Sigma$ of galaxies in the BOSS LOWZ and CMASS samples. Our main conclusion is that, it is viable for the combination of our standard HOD model and the best-fitting Planck ΛCDM cosmology to resolve the discrepancy between the large-scale galaxy bias and the small-scale g-g lensing signals, originally discovered by Leauthaud et al. (2017) for CMASS and subsequently for LOWZ (Lange et al. 2019).

We directly measure the LOWZ selection function of the central galaxies of the redMaPPer clusters, finding that the central selection function is largely independent of halo mass, at least in the cluster mass range. For the satellite galaxies, we developed a 2D galaxy selection function that allows the satellite detection fraction to decline from high completeness at high M_* to zero at low M_*, but with the characteristic stellar mass and width of the decline both dependent on the mass of the host haloes. Additionally, we carefully divide the galaxies of each redshift bin into three different stellar mass subsamples, so that each subsample covers a distinctive portion of the observed stellar mass distribution. This binning scheme allows us to better constrain the satellite fraction as a function of stellar mass from the large-scale w_p measurements.

We infer that the LOWZ magnitude and colour cuts select more low-M_* satellite galaxies from the high-M_h haloes, while the CMASS selection prefers low-M_* satellites from haloes with lower

mass. The CMASS preference also increases with increasing redshift, progressively selecting a higher fraction of low-M_* satellites at higher redshifts. Those inferred behaviours are consistent with the expectation that the blue fraction of satellites is a increasing function of redshift, but decreases with halo mass at fixed redshift. In particular, since the galaxy selection in LOWZ isolates the region of LRGs on the colour-magnitude diagram, the LOWZ selection prefers satellites from the more massive haloes. Meanwhile, the CMASS magnitude and colours cuts extend the selection to bluer populations at higher redshifts, hence the stronger preference of selecting satellites from low-mass haloes at high redshifts.

Overall, our best-fitting model provides excellent description of the observed number density and the project clustering of BOSS galaxies, and most important, a great match to the measured g-g lensing signals on scales below $1h^{-1}$Mpc for all the four redshift samples. On scales larger than $1h^{-1}$Mpc, similar to the findings in Leauthaud et al. (2017), the match is less ideal despite the relatively large measurement uncertainties, but there is little or no leeway for adjusting to a better fit without changing the cosmology. This is because the large-scale lensing is determined by the galaxy linear bias at any given cosmology, which is however tightly constrained by the high signal-to-noise w_p measurements. Therefore, it is unclear whether the large-scale lensing discrepancy will disappear with improved lensing measurements in the future, or requires modifications to cosmology or adding even new physics. As to our remedy to the small-scale lensing discrepancy, we anticipate that the stellar-mass complete galaxy samples observed by DESI (DESI Collaboration et al. 2016) and PFS (Takada et al. 2014) would provide a more conclusive and complete answer to the validity of our model.

ACKNOWLEDGEMENTS

We thank Johannes Lange for providing the LOWZ lensing measurements, Jesse Golden-Marx for the assistance with running `EzGal`, Hong Guo for the help understanding the BOSS data set, and Ben Wibking for the stimulating discussions. YZ acknowledges the support by the National Key Basic Research and Development Program of China (No. 2018YFA0404504), National Science Foundation of China (11621303, 11873038), the National One-Thousand Youth Talent Program of China, the STJU start-up fund (No. WF220407220), and the "111" project of the Ministry of Education under grant No. B20019. YZ also thanks the hospitality of Cathy Huang during his visit to Zhangjiang Hi-Tech Park that inspired this project.

REFERENCES

Aihara H., et al., 2011, ApJS, 193, 29
Alam S., et al., 2015, ApJS, 219, 12
Alam S., et al., 2017, MNRAS, 470, 2617
Anderson M. E., Gaspari M., White S. D. M., Wang W., Dai X., 2015, MNRAS, 449, 3806
Behroozi P. S., Conroy C., Wechsler R. H., 2010, ApJ, 717, 379
Berlind A. A., Weinberg D. H., 2002, ApJ, 575, 587
Bolton A. S., et al., 2012, AJ, 144, 144
Bruzual G., Charlot S., 2003, MNRAS, 344, 1000
Bundy K., et al., 2015, ApJS, 221, 15
Bundy K., Leauthaud A., Saito S., Maraston C., Wake D. A., Thomas D., 2017, ApJ, 851, 34
Cerulo P., Orellana G. A., Covone G., 2019, MNRAS, 487, 3759
Chabrier G., 2003, PASP, 115, 763
Chandrasekhar S., 1943, ApJ, 97, 255
Charlot S., Fall S. M., 2000, ApJ, 539, 718
Chen Y.-M., et al., 2012, MNRAS, 421, 314
Conroy C., Wechsler R. H., Kravtsov A. V., 2006, ApJ, 647, 201
Cooper M. C., et al., 2007, MNRAS, 376, 1445
DESI Collaboration et al., 2016, arXiv e-prints, p. arXiv:1611.00036
Davis M., Peebles P. J. E., 1983, ApJ, 267, 465
Dawson K. S., et al., 2013, AJ, 145, 10
Eisenhardt P. R. M., Lebofsky M. J., 1987, ApJ, 316, 70
Eisenstein D. J., et al., 2001, AJ, 122, 2267
Eisenstein D. J., et al., 2011, AJ, 142, 72
Foreman-Mackey D., Hogg D. W., Lang D., Goodman J., 2013, PASP, 125, 306
Fukugita M., Ichikawa T., Gunn J. E., Doi M., Shimasaku K., Schneider D. P., 1996, AJ, 111, 1748
Gao L., White S. D. M., 2007, MNRAS, 377, L5
Gao L., Springel V., White S. D. M., 2005, MNRAS, 363, L66
García R., Rozo E., 2019, MNRAS, 489, 4170
Gunn J. E., et al., 1998, AJ, 116, 3040
Gunn J. E., et al., 2006, AJ, 131, 2332
Guo H., Zehavi I., Zheng Z., 2012, ApJ, 756, 127
Guo H., et al., 2016, MNRAS, 459, 3040
Guo H., Yang X., Lu Y., 2018, ApJ, 858, 30
Guzik J., Seljak U., 2002, MNRAS, 335, 311
Hansen S. M., Sheldon E. S., Wechsler R. H., Koester B. P., 2009, ApJ, 699, 1333
Jing Y. P., Suto Y., 2002, ApJ, 574, 538
Jing Y. P., Suto Y., Mo H. J., 2007, ApJ, 657, 664
Kroupa P., 2001, MNRAS, 322, 231
Landy S. D., Szalay A. S., 1993, ApJ, 412, 64
Lange J. U., van den Bosch F. C., Zentner A. R., Wang K., Villarreal A. S., 2019, MNRAS, 487, 3112
Leauthaud A., Tinker J., Behroozi P. S., Busha M. T., Wechsler R. H., 2011, ApJ, 738, 45
Leauthaud A., et al., 2016, MNRAS, 457, 4021
Leauthaud A., et al., 2017, MNRAS, 467, 3024
Mancone C. L., Gonzalez A. H., 2012, PASP, 124, 606
Mandelbaum R., Seljak U., Kauffmann G., Hirata C. M., Brinkmann J., 2006, MNRAS, 368, 715
Mandelbaum R., Wang W., Zu Y., White S., Henriques B., More S., 2016, MNRAS, 457, 3200
Maraston C., Strömbäck G., 2011, MNRAS, 418, 2785
Maraston C., Strömbäck G., Thomas D., Wake D. A., Nichol R. C., 2009, MNRAS, 394, L107
Masters K. L., et al., 2011, MNRAS, 418, 1055
Miyatake H., More S., Takada M., Spergel D. N., Mandelbaum R., Rykoff E. S., Rozo E., 2016, Phys. Rev. Lett., 116, 041301
Montero-Dorta A. D., et al., 2016, MNRAS, 461, 1131
Naab T., Ostriker J. P., 2017, ARA&A, 55, 59
Navarro J. F., Frenk C. S., White S. D. M., 1997, ApJ, 490, 493
Nishimichi T., et al., 2019, ApJ, 884, 29
Nishizawa A. J., et al., 2018, PASJ, 70, S24
Planck Collaboration et al., 2020, A&A, 641, A6
Reid B., et al., 2016, MNRAS, 455, 1553
Rodríguez-Torres S. A., et al., 2016, MNRAS, 460, 1173
Runge J., Yan H., 2018, ApJ, 853, 47
Rykoff E. S., et al., 2014, ApJ, 785, 104
Saito S., et al., 2016, MNRAS, 460, 1457
Shankar F., Lapi A., Salucci P., De Zotti G., Danese L., 2006, ApJ, 643, 14
Sheth R. K., Tormen G., 2004, MNRAS, 350, 1385
Simet M., McClintock T., Mandelbaum R., Rozo E., Rykoff E., Sheldon E., Wechsler R. H., 2017, MNRAS, 466, 3103
Smee S. A., et al., 2013, AJ, 146, 32
Takada M., et al., 2014, PASJ, 66, R1
Tinker J. L., Weinberg D. H., Zheng Z., Zehavi I., 2005, ApJ, 631, 41
Vale A., Ostriker J. P., 2006, MNRAS, 371, 1173
Wake D. A., et al., 2006, MNRAS, 372, 537
Wechsler R. H., Tinker J. L., 2018, ARA&A, 56, 435

Weinberg D. H., Mortonson M. J., Eisenstein D. J., Hirata C., Riess A. G., Rozo E., 2013, Phys. Rep., 530, 87
Wibking B. D., et al., 2019, MNRAS, 484, 989
Wibking B. D., Weinberg D. H., Salcedo A. N., Wu H.-Y., Singh S., Rodríguez-Torres S., Garrison L. H., Eisenstein D. J., 2020, MNRAS, 492, 2872
Yang X., Mo H. J., van den Bosch F. C., Zhang Y., Han J., 2012, ApJ, 752, 41
Yang L., Jing Y., Yang X., Han J., 2019, ApJ, 872, 26
Yoo J., Tinker J. L., Weinberg D. H., Zheng Z., Katz N., Davé R., 2006, ApJ, 652, 26
Yuan S., Eisenstein D. J., Leauthaud A., 2020, MNRAS, 493, 5551
Zhai Z., et al., 2019, ApJ, 874, 95
Zhao D. H., Jing Y. P., Mo H. J., Börner G., 2009, ApJ, 707, 354
Zheng Z., Weinberg D. H., 2007, ApJ, 659, 1
Zu Y., Mandelbaum R., 2015, MNRAS, 454, 1161
Zu Y., Mandelbaum R., 2016, MNRAS, 457, 4360
Zu Y., Mandelbaum R., 2018, MNRAS, 476, 1637
Zu Y., Weinberg D. H., 2013, MNRAS, 431, 3319
Zu Y., Weinberg D. H., Rozo E., Sheldon E. S., Tinker J. L., Becker M. R., 2014, MNRAS, 439, 1628
Zu Y., Mandelbaum R., Simet M., Rozo E., Rykoff E. S., 2017, MNRAS, 470, 551
van den Bosch F. C., More S., Cacciato M., Mo H., Yang X., 2013, MNRAS, 430, 725

This paper has been typeset from a TEX/LATEX file prepared by the author.